



11 **Reservoir-Induced Seismicity in China: Systematic Characterization**
12 **and Implications for Hazard Assessment**

13 Jiashan Zhang¹, Changsheng Jiang^{1,*}, Fengling Yin¹, Yiming Zhu¹, Hongyu Zhai¹,

14 Jinmeng Bi², Yan Zhang¹

15 ¹Institute of Geophysics, China Earthquake Administration, Beijing 100081, China

16 ²Tianjin Earthquake Agency, Tianjin 300201, China

17 **Correspondence: Changsheng Jiang (jiangcs@cea-igp.ac.cn)**

18

19 **Abstract:** Reservoir-Induced Seismicity (RIS) poses a significant geological risk for
20 large-scale hydropower projects. However, its nationwide characteristics remain poorly
21 understood in China, the country with the world's largest hydropower capacity. This
22 study integrates a high-resolution national reservoir dataset (CRD) with a unified
23 earthquake catalog since 1970 to establish the first screening sample of 1,435
24 large/medium-sized reservoirs (impounded between 1971 and 2015) in China. Based
25 on spatiotemporal clustering criteria, we systematically identified 88 induced-type
26 reservoirs. Analysis of this dataset reveals fundamental characteristics of RIS in China:
27 Spatially, induced-type reservoirs are selectively concentrated in tectonically active
28 regions like the eastern margin of the Tibetan Plateau, showing significant coupling
29 with active faults and historical seismicity. Temporally, 95% of RIS events occur within
30 24.8 km of the reservoir shoreline, and their occurrence rate and time lag (Time Lag)
31 follow patterns governed primarily by pore pressure diffusion, leading to the
32 development of a W-score model for probabilistic RIS identification. In terms of



33 sequence characteristics, RIS exhibits statistically distinct parameters (*e.g.*, lower α -
34 value, higher b -value) compared to natural earthquakes, revealing a unique physical
35 process of activating near-critical faults via pore pressure diffusion. The spatial
36 evolution of the b -value further confirms an effective permeability boundary of pore
37 water penetration at approximately 30-40 km, far exceeding the current Chinese
38 national standard (10 km). Correlation analysis shows that static reservoir parameters
39 are interdependent; thus, only one parameter should be selected for hazard analysis.
40 Reservoir capacity (Reservoir Capacity) greater than $3.2 \times 10^8 \text{ m}^3$ or reservoir major
41 axis length (Reservoir Major Axis) exceeding 15.9 km could serve as quantitative
42 thresholds for preliminary risk screening during the planning stage. However,
43 correlation matrix analysis reveals only weak correlations between all static/dynamic
44 parameters and the maximum magnitude (M_{\max}), highlighting the urgent need for
45 physics-based mechanistic models. This study provides the first systematic
46 characteristic map, a quantitative identification tool (W-score), and key engineering
47 thresholds for RIS risk assessment in China, pointing towards future directions beyond
48 traditional empirical models.

49 **Keywords:** Reservoir-induced seismicity, earthquake sequence parameters, pore
50 pressure diffusion, seismic hazard

51

52 **1 Introduction**

53 Reservoir-Induced Seismicity (RIS), a typical example of human engineering activities
54 altering the local crustal stress field and triggering seismic events, holds significant



55 engineering and scientific value (Gupta, 2002). From an engineering perspective, even
56 low-magnitude RIS can cause damaging shaking and social impact in steep terrain due
57 to its shallow source characteristics, potentially triggering secondary disasters like
58 rockfalls (Julian and Foulger, 2010). Scientifically, RIS provides a unique natural
59 laboratory for understanding the critical role of fluids in fault instability (Talwani, 1997).
60 While over 200 RIS cases have been reported globally (Zhu *et al.*, 2020), systematic,
61 national-scale studies remain relatively scarce, with only a few countries like Canada,
62 France, and Brazil having conducted comprehensive analyses based on their own data
63 (Lamontagne *et al.*, 2018; Grasso *et al.*, 2018; Barros *et al.*, 2018). These studies reveal
64 that RIS occurrence is not random but strongly controlled by the regional tectonic
65 setting. For instance, RIS in Canada is concentrated within the ancient, stable Canadian
66 Shield, associated with the reactivation of fragile faults from paleo-rifts, with a typically
67 limited affected area (<5 km, Lamontagne *et al.*, 2018). In France, RIS primarily occurs
68 in active tectonic zones like the Western Alpine Arc and the Pyrenees, and its spatial
69 distribution can be normalized using the reservoir major axis length (Reservoir Major
70 Axis) as a characteristic scale (Grasso *et al.*, 2018). Research in Brazil further indicates
71 that the probability of RIS is significantly higher in areas with high natural seismicity
72 ($PGA > 0.1g$), suggesting that a critically stressed crust is a key prerequisite (Barros *et*
73 *al.*, 2018). These regional systematic studies have greatly enhanced our understanding
74 of RIS patterns, but their conclusions are derived from specific, mostly moderately to
75 low-active tectonic settings. A consequent key scientific question arises: whether these
76 patterns apply to the world's most active tectonic domains remains an urgent issue to



77 be addressed.

78 As the country with the largest global hydropower capacity, China has accumulated
79 valuable insights into RIS through case studies over the long term. The early case of
80 the Xinfengjiang Reservoir is a globally recognized typical RIS event. Recent studies
81 further revealed renewed intensification of seismicity northwest of the reservoir area
82 after 2012, interpreted as the reactivation of a pre-existing NW-SE trending fault due
83 to increased pore pressure from reservoir water infiltration ([Dong *et al.*, 2022](#)).

84 Research on the Three Gorges Reservoir uncovered complex spatiotemporal patterns
85 of its seismicity, which can be divided into near-field (0~12 km) and far-field (32~70
86 km) areas, possibly controlled by different mechanisms ([Li and Luo, 2022](#)). In the lower
87 reaches of the Jinsha River, impoundment of cascade reservoirs like Xiluodu and
88 Xiangjiaba was shown to alter the local stress field through the dual mechanisms of
89 "elastic loading and pore pressure diffusion," and was highly correlated in time and
90 space with a series of $M > 4.5$ earthquakes ([Miao *et al.*, 2025](#); [Zhang *et al.*, 2021](#)). These
91 case studies not only confirm the presence of RIS in China but also preliminarily
92 highlight the critical role of pore pressure diffusion in specific Chinese geological
93 environments (*e.g.*, areas with high-permeability faults and karst), where its influence
94 range may far exceed traditional understanding ([Miao *et al.*, 2025](#)).

95 Despite significant progress in case studies, the systematic patterns of RIS at the
96 national scale in China remain unclear. Due to the lack of a unified, high-precision
97 coupled dataset of national reservoirs and earthquakes, fundamental scientific questions
98 persist: To what extent is the spatial distribution of RIS controlled by macro-tectonic



99 patterns? What are the common characteristics of its spatiotemporal evolution? Do
100 sequence behaviors exhibit nationwide statistical fingerprints? What are the
101 quantitative influences of static or dynamic reservoir parameters on seismic activity?
102 This knowledge gap directly hampers the precision of engineering practice. China's
103 current risk assessment standards largely rely on early international experience and
104 static models. Whether their core parameters (*e.g.*, the 10 km influence range) are
105 universally applicable in China's complex and diverse geological environments,
106 especially in the southwestern region with widely developed high-permeability faults,
107 has become a critical issue requiring urgent verification. Addressing the above
108 questions, this study makes the first attempt to draw a more comprehensive
109 "characteristic map" for RIS in China. We integrated the high-resolution China
110 Reservoir Dataset (CRD) with a unified national earthquake catalog spanning over fifty
111 years to construct a screening sample of 1,435 large/medium-sized reservoirs (first
112 impounded between 1971/01/01 and 2015/03/27). Using unified spatiotemporal
113 clustering criteria, we systematically identified 88 induced-type reservoirs. Based on
114 this, to date, the most complete national-scale RIS dataset, this paper aims to
115 systematically address the following core questions: the spatial distribution pattern of
116 RIS in China and its coupling with regional tectonic background; the dominant
117 mechanism of RIS occurrence; whether the statistical parameters (*e.g.*, α -value, b -value,
118 and p -value) of RIS sequences are fundamentally different from those of natural
119 earthquakes; and the correlations between various static reservoir attributes (*e.g.*,
120 reservoir capacity (Reservoir Capacity), dam height (Dam Height)) and dynamic



121 response parameters (*e.g.*, distance from the reservoir shoreline of the M_{\max} event (M_{\max}
122 Distance), time lag of the M_{\max} event (Time Lag)) with the RIS maximum magnitude.
123 The results of this study will provide insights into the macroscopic patterns of RIS in
124 the world's most active tectonic domain and contribute to the development of more
125 physics-based risk assessment methods.

126 **2 Data Sources and Screening Sample Construction**

127 This study utilizes seismic data from the National Unified Official Earthquake Catalog
128 provided by the China Earthquake Networks Center (CENC,
129 <http://10.5.160.18/console/exit.action>, last accessed on April 15, 2025). The catalog
130 spans from January 1, 1970, to March 27, 2025, and contains basic parameters for all
131 earthquakes recorded by the national and regional seismic networks within China's
132 territory. Compiled and processed centrally by the CENC, this catalog integrates
133 observation reports from provincial and national centers to produce a unified
134 earthquake catalog and report (Dai *et al.*, 2019). The seismic monitoring capability,
135 represented by the minimum completeness magnitude (M_C), of the China Seismograph
136 Network has evolved significantly since 1970. For eastern China, where reservoirs are
137 densely distributed, the M_C was approximately M_L 3.0~3.5 in the 1970s, improved to
138 M_L 2.0~2.5 during 1980~2001, and after the nationwide digital upgrade of the network
139 around 2009, the M_C reached or even fell below M_L 2.0 in most regions (Mignan *et al.*,
140 2013; Wang *et al.*, 2017). This macroscopic evolution of monitoring capability and the
141 actual recorded data were considered during the identification of induced seismicity
142 sequences for individual reservoirs. Although obtaining the more complete, lower M_C



143 data recorded by dedicated seismic networks at individual reservoir sites is challenging,
144 the National Unified Official Earthquake Catalog used herein offers significant
145 advantages: it provides relatively consistent quality coverage across China and a long-
146 term record spanning over 50 years since 1970.

147 The spatial distribution and fundamental attributes of reservoirs are primarily sourced
148 from the China Reservoir Dataset (CRD; [Song et al., 2022](#)). The CRD is a
149 comprehensive dataset constructed based on the interpretation of high-resolution
150 satellite imagery, providing vector boundaries and key attributes—including name,
151 geographic location, reservoir capacity (Reservoir Capacity), reservoir surface area
152 (Reservoir Area), and administrative region—for 97,435 reservoirs across China.
153 Compared to mainstream international databases (*e.g.*, GeoDAR, GOODD, GRanD,
154 and Hi-Quake), the CRD offers significant advantages in terms of reservoir coverage,
155 spatial resolution, and attribute completeness within China ([Song et al., 2022](#)). This
156 dataset is indispensable for accurately delineating reservoir areas and investigating the
157 characteristics of reservoir-induced seismicity.

158 Critical parameters for identifying RIS, such as the initial impoundment time, dam
159 height (Dam Height), and Reservoir Capacity, were obtained through the integration of
160 multi-source, heterogeneous data. We systematically collected publicly available
161 academic literature, sources like the *Encyclopedia of Chinese Rivers and Lakes*, local
162 gazetteers, government reports, and news archives. For the 4,854 medium and large
163 reservoirs (Reservoir Capacity $\geq 0.1 \times 10^8 \text{ m}^3$) contained in the CRD, we performed
164 rigorous cross-validation and data fusion, resulting in a dataset of 1,435 reservoirs with



165 complete information for the aforementioned parameters. Due to limitations in data
166 availability, the precision of the obtained initial impoundment times varies. For times
167 precise only to the month, the last day of that month was taken as the initial
168 impoundment time; for times precise only to the year, January 1 of the following year
169 was used. This dataset is nearly complete for large reservoirs (Reservoir Capacity \geq
170 1×10^8 m³) nationwide, comprising 746 reservoirs, accounting for 84.29% of the
171 corresponding large reservoirs in the CRD. For medium reservoirs, 2,111 were
172 compiled, representing 53.39% of the corresponding medium reservoirs in the CRD.
173 Among the 1,997 reservoirs with incomplete records, 1,433 (71.76%) have a Reservoir
174 Capacity below 0.3×10^8 m³. As this study requires comparing seismic activity for at
175 least one year before initial impoundment and examining seismicity for at least ten
176 years after impoundment, only those 1,435 reservoirs with initial impoundment dates
177 between January 1, 1971, and March 27, 2015, were selected as the target group for
178 identifying induced seismicity.

179 **3 Identification of Induced Seismicity and Distribution Characteristics of** 180 **Induced-Type Reservoirs**

181 Similar to other types of human-induced seismicity, there is no deterministic method
182 for identifying Reservoir-Induced Seismicity (RIS). Current approaches primarily rely
183 on assessing the spatiotemporal correlation between seismic activity and anthropogenic
184 activities. We defined three concurrent criteria for identifying RIS: (1) The frequency
185 of seismic activity is significantly influenced by reservoir impoundment/operation,
186 particularly evidenced by a rapid increase in the frequency and intensity of seismicity



187 after initial impoundment, clearly distinguishable from the background seismicity
188 observed before impoundment. (2) The seismic activity exhibits clear spatial clustering,
189 often with linear geometric features consistent with fault activation. (3) The earthquake
190 clusters are located close to the reservoir area, demonstrating a clear spatial association.
191 As this study focuses on the overall statistical characteristics of RIS, we did not employ
192 quantitative probabilistic methods like the spatiotemporal Epidemic-Type Aftershock
193 Sequence (ETAS) model (Zhuang *et al.*, 2002) or the nearest neighbor distance (NND)
194 method (Zaliapin *et al.*, 2008) for cluster identification. Instead, we adopted an
195 approach similar to Bi and Jiang (2019), manually selecting the natural boundaries of
196 spatiotemporal earthquake clusters. Operationally, we examined seismic events within
197 50 km of the reservoir shoreline to identify clusters and then screened them against the
198 three criteria above to select RIS sequences. Reservoirs with clearly identified induced
199 seismicity are termed "induced-type reservoirs" in this study, and their corresponding
200 seismic sequences are termed "reservoir-induced seismicity sequences."
201 [Figure 1](#) shows an example of RIS identification for the Jinping-I Reservoir. Located
202 on the main stream of the Yalong River in Yanyuan and Muli counties, Liangshan
203 Prefecture, Sichuan Province, China, this reservoir is a key component of the Jinping-I
204 Hydropower Station. It has a total Reservoir Capacity of 7.76 billion cubic meters,
205 serves annual regulation functions, and provides comprehensive benefits including
206 power generation, flood control, and sediment retention. Initial impoundment began at
207 09:26 on November 30, 2012. Within the following year, significant earthquake
208 clustering occurred around the reservoir ([Figure 1a](#)). Notably, two distinct seismic



209 clusters emerged near the central part and the western end (tail) of the reservoir, close
210 to the shoreline, with a maximum magnitude of M_S 4.3. These two clusters, delineated
211 by purple dashed polygons in [Figure 1a](#), were manually selected as candidate induced
212 sequences. Analyzing the distance-from-shoreline distribution for earthquakes within
213 these clusters, selected using completeness magnitudes (M_C) of M_L 2.0, 2.5, and 3.0,
214 revealed similar characteristics: events were primarily concentrated within 0~12 km of
215 the shoreline, with a peak distribution at 4~5 km ([Figure 1b](#)). Similarly, examining the
216 temporal evolution of the cumulative frequency for these candidate sequences (using
217 different M_C thresholds) and comparing it with the cumulative frequency of background
218 seismicity (unselected events within 50 km) and all earthquakes in the area, shows a
219 distinct increase in the candidate sequences starting around 250 days after
220 impoundment. This increase clearly distinguishes them from the background seismicity,
221 the total seismicity, and the pre-impoundment background activity ([Figure 1c](#)). This
222 consistency satisfies the three identification criteria proposed herein. Therefore, the
223 Jinping-I Reservoir is classified as an induced-type reservoir, and the selected
224 sequences are identified as RIS sequences. As the spatiotemporal patterns remain
225 consistent across different M_C values, indicating the stability of the identification results,
226 we used the sequences filtered with $M_C = M_L 2.5$ —considering the completeness of the
227 catalog in the reservoir area—as the dataset for subsequent analysis. Applying the
228 above RIS identification methodology to the 1,435 large/medium reservoirs in the study
229 period, we identified 88 induced-type reservoirs, comprising 56 large reservoirs and 32
230 medium reservoirs. Their spatial distribution is shown in [Figure 2a](#), and basic



231 information is listed in [Table 1](#).

232 Conventional understanding suggests that the occurrence mechanisms of RIS are

233 closely related to the regional tectonic setting, and their spatial distribution contains key

234 information about the triggering mechanisms. For instance, [Lamontagne *et al.* \(2018\)](#)

235 found that RIS in Canada is concentrated within the Quebec Canadian Shield,

236 potentially related to the reactivation of fragile faults remnant from the Precambrian rift

237 period under the influence of pore pressure diffusion from reservoir water. [Grasso *et al.*](#)

238 [\(2018\)](#) observed that RIS in France is mainly concentrated in tectonic zones like the

239 Western Alpine Arc, Pyrenees, and Rhine Graben, attributing this pattern to high

240 tectonic stress accumulation caused by stress fields near microplate boundaries. [Barros](#)

241 [et al.](#) (2018) found that RIS in Brazil is spatially concentrated along the edges of the

242 São Francisco Craton, within the basaltic rocks of the Paraná Basin, and near orogenic

243 belt boundaries, with a significantly higher probability of occurrence in regions of

244 strong natural tectonic seismicity ($PGA > 0.1g$). Understanding the spatial distribution

245 patterns of induced-type reservoirs and their relationship with geological structures and

246 regional seismicity is fundamental for revealing RIS triggering mechanisms and

247 assessing regional RIS hazard.

248 Based on the 88 identified induced-type reservoirs, we systematically analyzed their

249 spatial distribution characteristics. The results indicate a pronounced regional clustering

250 of induced-type reservoirs in China, predominantly concentrated in the tectonically

251 most active southwestern region, especially central Sichuan-Yunnan rhombic block and

252 southwestern Yunnan, with only sporadic occurrences in southeastern coastal and



253 northeastern regions (Figure 2a). This spatial pattern is highly consistent when viewed
254 in terms of the density (number per unit area) of induced-type reservoirs (Figure 2b)
255 and their proportion relative to all large/medium reservoirs within a region (Figure 2c).
256 The southwestern region is not only the core area of China's hydropower resources and
257 the most densely populated area for large/giant reservoirs but also has the highest
258 identified proportion of induced-type reservoirs, highlighting the elevated risk of
259 induced seismicity for large reservoirs in specific tectonic environments. Further
260 comparison with the regional tectonic background (active faults since the Late
261 Pleistocene) and the spatial distribution of moderate-to-strong seismicity ($M \geq 4.0$)
262 earthquakes since 1970, Figure 2d) reveals a significant spatial correlation between the
263 distribution of induced-type reservoirs and areas of active tectonics and seismicity.
264 Therefore, compared to the overall distribution of large/medium reservoirs nationwide,
265 the spatial distribution of induced-type reservoirs is highly selective and primarily
266 controlled by regional tectonic activity intensity. In particular, the strong crustal
267 deformation, high tectonic stress accumulation, and widely developed active fault
268 systems along the eastern margin of the Tibetan Plateau provide favorable mechanical
269 conditions and pathways for reservoir water infiltration, fault weakening, and
270 earthquake triggering. In contrast, the relatively stable tectonic eastern plains, despite
271 having numerous reservoirs, show a significantly lower incidence of induced seismicity.
272 This marked spatial correlation reveals the non-uniformity of reservoir-induced seismic
273 hazard at the regional scale, an important aspect to be considered in the planning and
274 siting of future major water conservancy and hydropower projects, regional seismic



275 hazard assessments, and the development of operational risk monitoring strategies.

276 **4 Spatiotemporal Characteristics of Induced Seismicity Sequences**

277 The spatiotemporal distribution patterns of induced seismicity sequences are closely
278 related to their triggering mechanisms, and empirical understanding has been
279 established in some countries and regions. For example, all RIS events in Canada are
280 concentrated within 5 km of the reservoir shoreline, related to the permeability of faults
281 near the reservoir and the localized effect of pore pressure diffusion ([Lamontagne *et al.*,
282 2018](#)). In France, the spatial distribution of RIS can be normalized using the reservoir
283 major axis length (Reservoir Major Axis) as a characteristic scale, with the earthquake
284 occurrence rate within 1~3 times the Reservoir Major Axis being 4.5 times higher than
285 in the far-field (10 times the Reservoir Major Axis), confirming the localized nature of
286 tectonic stress perturbation ([Grasso *et al.*, 2018](#)). Regarding the time lag (Time Lag)
287 between RIS occurrence and the initial impoundment, previous studies found that RIS
288 in Canada is predominantly characterized by a delayed response, where the Time Lag
289 is negatively correlated with fault permeability ([Lamontagne *et al.*, 2018](#)). In France,
290 62% of RIS events occur within 2 years after impoundment, corresponding to a rapid
291 response to elastic loading, consistent with [Simpson *et al.* \(1988\)](#) Type I model ([Grasso
292 *et al.*, 2018](#)). A systematic understanding of the spatiotemporal patterns of RIS in China
293 has not yet been established.

294 Based on the identified induced seismicity sequences from the 88 reservoirs, this study
295 uses a completeness magnitude of $M_L 2.5$ and a sequence duration of 10 years after
296 initial impoundment to investigate the distance-from-shoreline distribution and Time



297 Lag distribution characteristics of RIS. Since the occurrence rate varies significantly
298 among different RIS sequences, we normalized the frequency for each sequence to
299 extract common patterns. Specifically, the earthquake frequency in each distance or
300 time bin was divided by the total number of earthquakes in the respective RIS sequence,
301 so that the sum of normalized frequencies (relative frequencies) for all bins equals 1,
302 intuitively reflecting the proportion of earthquakes in each bin. The statistical
303 distributions from all RIS sequences were then stacked and normalized again. The
304 resulting composite distance-from-shoreline and Time Lag distribution characteristics
305 for all RIS sequences are shown in [Figures 3a](#) and [3b](#), respectively.

306 The results show that RIS sequences are closely distributed around the reservoir area.
307 The cumulative frequency of earthquakes along the distance from the shoreline reaches
308 95% at 24.8 km and 99% at 38.2 km. This indicates that the maximum distance of RIS
309 sequences can approach 40 km, suggesting that the influence range stipulated within 10
310 km of the reservoir area in the current Chinese national standard GB 21075-2007
311 (*Reservoir-Induced Seismic Hazard Assessment*) is overly conservative and may
312 underestimate the spatial extent required for risk prevention and control. More
313 importantly, [Figure 3a](#) shows that the earthquake occurrence rate of RIS sequences
314 follows a significant power-law decay with increasing distance from the reservoir
315 shoreline. This characteristic highly aligns with theoretical models of fault activation
316 by fluid infiltration and diffusion ([Talwani, 1997](#)), revealing that the primary physical
317 mechanism for RIS in China is related to pore pressure diffusion. This is because the
318 pore pressure increase caused by reservoir impoundment diffuses through pre-existing



319 fractures, faults, and pores in the rock mass. The combined effect of the diffusion front
320 and the nonlinear dependence of triggering probability on pressure changes typically
321 results in a power-law decay of the probability or occurrence rate of triggered seismicity
322 with distance.

323 Temporally, [Figure 3b](#) shows that the seismic frequency of RIS sequences gradually
324 increases after initial impoundment, peaks within 1~2 years, and then gradually decays.

325 This delayed response and gradual increase are typical manifestations of the time
326 required for pore pressure diffusion. Reservoir water infiltrates downward and outward
327 through pores, fractures, and pre-existing fault networks in the rock, causing pore
328 pressure perturbations to propagate at a rate controlled by the hydraulic diffusivity.

329 Significant increase in seismicity occurs only when the pore pressure front reaches and
330 sufficiently increases the effective pore pressure in deep potential fault zones to meet
331 the critical failure condition. The decay after the peak reflects stress release from the
332 most easily triggered fault ruptures in areas reached early by the pressure front. As the
333 diffusion distance increases, the pressure perturbation gradient decreases, and the
334 efficiency of infiltration paths reduces, making it more difficult to trigger new
335 earthquakes. The temporal evolution of RIS typically involves two potential
336 mechanisms ([Talwani, 1997](#)). One is the instantaneous elastic stress change due to
337 reservoir water load, which may trigger near-field, shallow earthquakes within a very
338 short time (hours to weeks) after impoundment. The other is pore pressure diffusion,
339 which triggers earthquakes on a timescale of months to years. The observed significant
340 delayed increase (month scale) and peak (year scale) clearly indicate that pore pressure



341 diffusion is the dominant mechanism. The potential contribution of early elastic loading,
342 triggering very few near-field events, is ~~微弱~~ (weak) in the overall statistical
343 characteristics of the sequences.

344 To quantitatively characterize the spatiotemporal coupling features of RIS, this study
345 adopted the W-score method from Ghofrani and Atkinson (2020). Based on the spatial
346 and temporal evolution characteristics described above, we constructed a power-law
347 decay distribution function for the distance from the shoreline (d) and a hybrid power-
348 law and linear distribution function for the Time Lag (t). Empirical functions were
349 obtained by fitting the actual data as follows:

$$350 \quad f(d)=0.118e^{-0.121d} \quad (1)$$

$$351 \quad f(t)= -0.107e^{-5.686t}-0.003t+0.039 \quad (2)$$

352 Assuming equal weight for the empirical function of distance (d) and the empirical
353 function of Time Lag (t), the comprehensive W-score formula was established as
354 follows:

$$355 \quad W= \frac{\{f(d)+f(t)\}}{2} \quad (3)$$

356 [Figure 3c](#) shows the two-dimensional W-score results described by equation (3). The
357 W-score at any location in the figure represents the probability of any earthquake event
358 being induced, thus enabling a quantitative assessment of the probability of RIS. [Figure](#)
359 [3d](#) shows an example application of the W-score to the RIS sequence at the Jinping-I
360 Reservoir ([Figure 1](#)). It can be seen that the RIS sequence is significantly clustered in
361 high W-value regions ($0.6 < W < 1.0$), while background natural tectonic earthquakes
362 are mainly distributed in low W-value regions ($W < 0.4$). This W-score table provides



363 a new quantitative analysis tool for identifying RIS in China.

364 **5 Parameter Characteristics of Induced Seismicity Sequences**

365 The statistical parameters of reservoir-induced seismicity sequences contain key
366 information about their triggering mechanisms and evolution processes. For example,
367 the b -value in the magnitude-frequency relationship describes the differential stress
368 level (Jiang *et al.*, 2021; Yin and Jiang, 2024; Chang *et al.*, 2025); the p -value in the
369 Omori-Utsu formula describes the decay rate of a sequence (Trivedi, 2015; Utsu, 1999);
370 and the α -value in the Epidemic-Type Aftershock Sequence (ETAS) model describes
371 the ability of an earthquake to generate secondary events (Ogata, 1988; Bi and Jiang,
372 2019). To systematically reveal the characteristics and physical implications of RIS
373 sequences in China, this study calculated the α -value, b -value, and p -value using the
374 identified induced seismicity sequences from reservoirs impounded between January 1,
375 1971, and March 27, 2015, and compared them with parameters of natural earthquake
376 sequences. Additionally, we compared the b -value of the RIS sequences with the
377 background seismicity in the respective reservoir areas.

378 For the b -value calculation, we followed the approach of Yin and Jiang (2024), using
379 the continuous distribution function given by Ogata and Katsura (1993) to describe the
380 magnitude-frequency distribution (FMD), hereafter referred to as the OK1993 model:

$$381 \quad \lambda(\beta/m) = e^{-\beta m} \frac{1}{\sqrt{2\pi\sigma^2}} \int_{-\infty}^M e^{-\frac{(x-u)^2}{2\sigma^2}} dx, \quad (4)$$

382 where M is the maximum magnitude in the earthquake catalog used for calculation, and
383 the power-law exponent β is related to the traditional G-R relation b -value by
384 $\beta = b \cdot \log 10$. Specifically, the value of β was obtained by fitting the log-likelihood



385 function of the OK1993 model using the maximum likelihood method, and the b -value
386 was subsequently estimated.

387 We used the time-dependent Epidemic-Type Aftershock Sequence (ETAS) model to
388 calculate the parameters p -value and α -value. The conditional intensity function of the
389 ETAS model can be expressed as (Ogata, 1988):

$$390 \quad \lambda(t) = \mu + K \sum_{t_i < t} \frac{e^{\alpha(M_i - M_0)}}{(t - t_i + c)^p}, M_i > M_0 \quad (5)$$

391 In the above equation, t is the time after the mainshock, M_0 is the cutoff magnitude; M_i
392 and t_i are the magnitude and occurrence time of the i -th event, respectively, μ is the
393 background seismicity rate of the source region, c is the time after the mainshock when
394 the aftershock frequency peaks, and the constant K represents the productivity of
395 aftershocks. The p -value for natural tectonic earthquakes is typically around 1.0, and
396 the α -value is generally greater than 1.0 but is usually less than 1.0 for swarm-like
397 sequences (Ogata, 2001). Limited by an insufficient number of earthquakes ($N < 40$) in
398 some RIS sequences or large uncertainties in the sequence parameters (δb , δp , $\delta \alpha >$
399 parameter/10), we successfully calculated the corresponding parameters for 38 RIS
400 sequences.

401 The statistical distributions of the calculated α -values, b -values, and p -values are shown
402 in Figures 4a~c. The median α -value is 0.89, the median b -value is 1.16, and the median
403 p -value is 1.11. To compare with the statistical characteristics of natural earthquake
404 sequence parameters, we collected 66 cases from previous studies that also used the
405 time-dependent ETAS model for fitting and provided the resulting parameters (Jiang *et*
406 *al.*, 2013a, 2013b, 2014; Guo, 2015; Bi and Jiang, 2019; Mesimeri *et al.*, 2019; Xue *et*



407 *al.*, 2021). These cases are mainly from China (51 cases) and partially from other
408 regions globally (15 cases). All provide calculated p -values and α -values, and some
409 provide b -value results (31 cases). The median α -value for these natural sequences is
410 1.88, the median b -value is 0.83, and the median p -value is 1.10. The corresponding
411 parameter values are listed in Table 2. Direct comparison of the statistical distributions
412 of α -value, b -value, and p -value shows that the α -values of RIS sequences are generally
413 smaller than those of natural sequences, the b -value distribution is more scattered and
414 generally higher, and the p -values are relatively similar. We used the Kolmogorov-
415 Smirnov test (significance level $P=0.05$) to examine whether the respective parameter
416 combinations of RIS sequences and natural sequences come from the same distribution.
417 The results show significant differences for b -value and α -value (significance level $P <$
418 0.05), while the difference for p -value is not statistically significant (significance level
419 $P = 0.461 \gg 0.05$). Furthermore, to avoid potential intrinsic correlations among these
420 parameters (e.g., Wang, 1994; Jiang *et al.*, 2015) affecting the distinguishability
421 between RIS and natural sequence characteristics, we examined the pairwise
422 distribution relationships among the three sequence parameters. As shown by the
423 sample density contour plots in Figures 4d~f, the distribution of RIS sequence
424 parameters can be clearly distinguished from that of natural earthquake sequence
425 parameters in the combined distributions of b -value vs. α -value, b -value vs. p -value,
426 and p -value vs. α -value. Therefore, it can be concluded that RIS sequences and natural
427 earthquake sequences have distinct characteristics in their statistical parameters, mainly
428 manifested as: RIS sequences typically have higher b -values (indicating lower effective



429 stress/higher proportion of small earthquakes) and significantly lower α -values
430 (indicating weaker ability of small-magnitude events to trigger secondary earthquakes).
431 These differences may reveal the fundamental distinctions between the triggering
432 mechanism (dominated by pore pressure diffusion) and evolution process (rapid decay,
433 weaker triggering ability of large earthquakes) of RIS compared to natural earthquakes.
434 To further investigate the differences between RIS sequences and the background
435 seismicity around the reservoir areas, this study compared the b -value of the induced
436 sequence with the b -values of background seismicity at different distances from the
437 reservoir shoreline (Figure 5). We employed two spatial strategies: The first was a
438 concentric zoning strategy, dividing the area around the reservoir into concentric zones
439 of 0~10 km, 10~20 km, 20~30 km, 30~40 km, and 40~50 km. The b -value of
440 background seismicity in each zone was calculated independently and compared with
441 the RIS sequence b -value using the KS test (significance level $P=0.05$). The results
442 show that the P for all zones are greater than 0.05, indicating no significant difference
443 was identified. The second was a cumulative zoning strategy, gradually expanding the
444 study area in 10 km increments (0~10 km \rightarrow 0~50 km). The b -value of background
445 seismicity within the cumulative range was calculated. The KS test results show that
446 the P decreases initially with increasing cumulative distance, becomes significantly
447 lower than 0.05 at 30 km and 40 km, indicating a significant difference between the
448 background seismicity b -value beyond this distance and the RIS sequence b -value. The
449 P increases again after 40 km, possibly because beyond the effective range of reservoir
450 water penetration, the background seismicity is controlled by the tectonic environment,



451 and the b -value stabilizes. These results suggest that a distance of 30 km to 40 km from
452 the shoreline may be a critical physical boundary, which can be defined as the effective
453 spatial scale of reservoir water penetration. The first strategy failed to identify a
454 difference, primarily due to insufficient sample size of far-field earthquakes and the
455 smoothing effect of spatial continuity.

456 **6 Correlation Analysis of Inducing Factors**

457 To further elucidate the potential factors influencing the intensity of RIS sequence
458 activity, we analyzed the correlation between the maximum magnitude (M_{\max}) of the
459 RIS sequences and two categories of parameters, totaling eight specific factors. The
460 first category comprises static reservoir attributes: reservoir capacity (Reservoir
461 Capacity, 10^8 m^3), dam height (Dam Height, m), reservoir surface area (Reservoir Area,
462 km^2), reservoir major axis length (Reservoir Major Axis, km), and mean water depth
463 (Capacity / Area, m), the latter calculated as Reservoir Capacity / Reservoir Area. The
464 second category describes the dynamic response of RIS: the distance from the reservoir
465 shoreline of the M_{\max} event (M_{\max} Distance, km), the time lag of the M_{\max} event since
466 initial impoundment (Time Lag, days), and the time lag of the peak seismicity rate since
467 initial impoundment (Peak Lag, days). It is important to note that since dynamic
468 response parameters cannot be defined for non-induced reservoirs, this analysis is based
469 solely on the sample of 88 induced-type reservoirs. To comprehensively analyze the
470 potential correlations with M_{\max} , we employed both the Pearson correlation coefficient
471 (r) (Pearson, 1895), suitable for linear correlation analysis, and the Spearman
472 correlation coefficient (ρ) (Spearman, 1904), suitable for non-linear monotonic



473 correlation analysis. The Pearson correlation coefficient is a statistic based on linear
474 relationships, measuring the strength of linear correlation by calculating the
475 standardized covariance. Its value ranges from [-1, 1], with positive values indicating a
476 positive correlation and negative values a negative correlation (Pearson, 1895). Its
477 mathematical expression is:

$$478 \quad r = \frac{\sum(x_i - \bar{x})(y_i - \bar{y})}{\sqrt{\sum(x_i - \bar{x})^2 \sum(y_i - \bar{y})^2}} \quad (6)$$

479 The Spearman correlation coefficient is a non-parametric rank-based coefficient used
480 to capture non-linear monotonic relationships, particularly suitable for non-normally
481 distributed data or data containing outliers (Spearman, 1904). Its mathematical
482 expression is:

$$483 \quad \rho = 1 - \frac{6 \sum d_i^2}{n(n^2 - 1)} \quad (7)$$

484 In the above equations, x represents the logarithmically transformed inducing factor,
485 y represents the maximum magnitude, and d_i is the difference in ranks. Using these two
486 methods in combination allows for the identification of both linear trends and non-
487 linear monotonic relationships, with significance testing ($P < 0.05$ considered
488 significant) ensuring robust conclusions.

489 The results of the correlation analysis between the eight potential inducing factors and
490 M_{\max} are shown in Figure 6. The results indicate that the five static reservoir attribute
491 parameters exhibit weak positive correlations with M_{\max} . The Pearson correlation
492 coefficient (r) values range from 0.20 to 0.28, and the Spearman correlation coefficient
493 (ρ) values range from 0.21 to 0.32. For each parameter, at least one of the r or ρ values
494 has a significance level less than 0.05. In contrast, the three dynamic attribute



495 parameters show no correlation with M_{\max} , with r or ρ values close to zero, and the
496 corresponding significance levels all exceed 0.05. These results suggest that relying on
497 any single static or dynamic reservoir attribute parameter is insufficient for reliably
498 predicting the maximum magnitude (M_{\max}) of RIS. The physical mechanism underlying
499 this is that M_{\max} is primarily controlled by the pre-existing stress state and rupture scale
500 of local faults (Talwani, 1997), rather than by the properties of the reservoir itself. The
501 static reservoir parameters mainly modulate the timing of earthquake triggering through
502 the process of pore pressure diffusion.

503 Although the static and dynamic reservoir parameters show only weak or no correlation
504 with the intensity (M_{\max}) of the RIS sequences, whether these parameters can be used
505 for preliminary screening of induced seismic risk prior to reservoir construction remains
506 a valuable question. We address this from two perspectives. First, we examine whether
507 thresholds exist for the five static parameters that show weak but statistically significant
508 correlations, which could indicate high RIS risk. For this purpose, we binned the values
509 of the five static reservoir attribute parameters and examined the proportion of induced-
510 type reservoirs within each bin. The results are shown in Figure 7. Reservoir Capacity
511 and Reservoir Major Axis show clear threshold indicative value for the occurrence
512 probability of induced-type reservoirs: As shown in Figure 7b, when the Reservoir
513 Capacity exceeds $3.2 \times 10^8 \text{ m}^3$ ($10^{2.5} \times 10^8 \text{ m}^3$), the proportion of induced-type reservoirs
514 approaches 15%, which is already significant. In capacity bins above this threshold, the
515 proportion of induced-type reservoirs generally shows a positive correlation with
516 capacity. Figure 7c shows that the Reservoir Major Axis exhibits a similar characteristic;



517 when it exceeds 15.9 km ($10^{1.2}$ km), the proportion of induced-type reservoirs exceeds
518 11%. In length bins above this threshold, the proportion shows a positive correlation
519 with length. The existence of such clear thresholds in the proportion of induced-type
520 reservoirs for these two static parameters can provide a basis for preliminary screening
521 during project planning. Specifically, sites meeting or exceeding these threshold
522 conditions warrant specialized RIS hazard assessment.

523 Furthermore, to examine the independence or intercorrelation among the attribute
524 parameters, we calculated the Pearson correlation coefficient matrix (Figure 8) and the
525 Spearman correlation coefficient matrix (Figure 9) for all eight parameters. The results
526 show that the five static reservoir attribute parameters are relatively highly correlated
527 among themselves. The pairwise Pearson correlation coefficients (r) range from 0.39
528 to 0.95, and the Spearman correlation coefficients (ρ) range from 0.59 to 0.95. All are
529 positive correlations and statistically significant at the $P < 0.01$ level. This reflects the
530 inherent interrelationship among geometric parameters in hydropower project design
531 and highlights the need to focus on parameter independence when used in seismic
532 hazard analysis. The three dynamic reservoir attribute parameters show relatively
533 weaker correlations among themselves. The pairwise Pearson correlation coefficients
534 (r) range from 0.23 to 0.38, and the Spearman correlation coefficients (ρ) range from
535 0.22 to 0.33, also all positive. Notably, the correlations between static and dynamic
536 attribute parameters are all negative. This implies that larger reservoir dimensions tend
537 to be associated with the M_{\max} event occurring closer to the reservoir shoreline (smaller
538 M_{\max} Distance) and within a shorter Time Lag after initial impoundment, and the peak



539 seismicity rate also tends to be reached sooner after impoundment (smaller Peak Lag).

540 **7 Discussion**

541 This study finds that induced-type reservoirs in China exhibit a high degree of spatial
542 selectivity, with the vast majority concentrated in the strong tectonic activity zone along
543 the eastern margin of the Tibetan Plateau, showing significant spatial coupling with
544 active faults since the Late Pleistocene and historical moderate-to-strong ($M \geq 4.0$)
545 seismicity. This finding resonates with conclusions from several regional systematic
546 studies worldwide, collectively highlighting the critical controlling role of the regional
547 tectonic background on the occurrence of RIS. In Canada, RIS is concentrated within
548 the relatively stable Canadian Shield, and its limited triggering range (< 5 km) is
549 attributed to the reactivation of fragile faults associated with paleo-rifts under reservoir
550 water infiltration (Lamontagne *et al.*, 2018). In France, RIS preferentially occurs in
551 active tectonic zones (*e.g.*, Alps, Pyrenees), and its spatial influence range can be
552 effectively normalized using the Reservoir Major Axis (Deng *et al.*, 2010; Grasso *et al.*,
553 2018). Studies in Brazil also indicate that the probability of RIS is twice as high in areas
554 of high natural seismicity compared to aseismic regions, further supporting the view
555 that a critically stressed crust is an important prerequisite for RIS occurrence (Barros *et*
556 *al.*, 2018). The high concentration of RIS along the eastern margin of the Tibetan
557 Plateau revealed in this study reinforces the global understanding that "high tectonic
558 stress accumulation and developed fault systems are prerequisite geological conditions
559 for RIS occurrence." Compared to the Canadian and French cases, RIS in China
560 exhibits a broader spatial influence range (95% of events within 24.8 km, 99% within



561 38.2 km of the shoreline). This difference may stem from the more complex intraplate
562 tectonic setting, widely developed deep-seated faults, and higher fault permeability in
563 China, which provide preferred pathways for the long-distance diffusion of pore
564 pressure (Talwani *et al.*, 2007; Miao *et al.*, 2025). Furthermore, the observed RIS
565 influence range far exceeds the 10 km specified in the current Chinese national standard
566 (GB 21075-2007), strongly suggesting that this parameter should be revised in future
567 risk assessments to prevent potential spatial underestimation of risk.

568 The sequence parameter analysis in this study provides statistical evidence for
569 distinguishing RIS from natural tectonic earthquakes. We found that Chinese RIS
570 sequences exhibit significantly higher b -values and lower α -values. A high b -value
571 typically indicates lower effective stress in the source region or more fractured media,
572 which aligns well with the physical mechanism of pore pressure diffusion reducing the
573 effective normal stress on faults, thereby activating a large number of small-scale faults
574 that are in a critical state (Talwani, 1997; Rajendran and Talwani, 1992). A low α -value
575 suggests a weaker ability of small-magnitude events to trigger secondary sequences,
576 revealing a fundamental difference in the energy release pattern between the RIS
577 triggering process and natural mainshock-aftershock sequences. These characteristics
578 are consistent with findings from studies of the Xiluodu-Xiangjiaba reservoirs on the
579 lower Jinsha River in China (Miao *et al.*, 2025) and are inherently linked to the
580 observation in French RIS sequences of a large difference between the magnitude of
581 the second-largest aftershock and the mainshock (Grasso *et al.*, 2018). However, studies
582 on a few cases in Brazil found no significant difference between the b -value of RIS



583 sequences and the local natural earthquake b -value (Barros *et al.*, 2018), which differs
584 from the traditional view that RIS has higher b -values (Gupta *et al.*, 1972). Such
585 regional differences suggest that the sequence characteristics of RIS may be influenced
586 by local geological conditions, rock mechanical properties, and subtle differences in
587 triggering mechanisms, necessitating consideration of regional applicability when
588 using statistical parameters for discrimination. Furthermore, the spatial evolution
589 analysis of the b -value in this study statistically validates an effective boundary for
590 reservoir water penetration at 30~40 km. This not only supports the physical
591 mechanism of RIS but also provides a referential spatial constraint for defining
592 monitoring and assessment ranges in risk evaluation.

593 Regarding the triggering mechanism, the spatiotemporal evolution characteristics of
594 RIS in China strongly support the dominant role of pore pressure diffusion. The peak
595 in seismic activity 1~2 years after impoundment, and the significant power-law decay
596 of the occurrence rate with distance from the reservoir shoreline (M_{\max} Distance), are
597 typical manifestations of the pore pressure diffusion process (Talwani, 1997; Cheng *et al.*,
598 *et al.*, 2012; Grasso *et al.*, 2018). This is very similar to the case of the Song Tranh 2
599 reservoir in Vietnam, where seismicity was triggered shortly after impoundment (rapid
600 response) but the increase persisted after water level drop due to the delayed effect of
601 pore pressure diffusion, clearly identified as a typical case of "rapid and delayed
602 triggering" (Gahalaut *et al.*, 2016). Similarly, in the cascade reservoirs on the lower
603 Jinsha River in China, detailed 3D finite element simulations show the combined action
604 of "elastic loading and pore pressure diffusion" dual mechanisms, with pore pressure



605 diffusion dominating the contribution to Coulomb stress changes (Miao *et al.*, 2025).
606 In terms of temporal response type, different regions globally show some variation: RIS
607 in France is predominantly rapid response (Type I), with 62% of events occurring
608 within 2 years of impoundment (Grasso *et al.*, 2018); whereas RIS in Canada and Brazil
609 more often exhibits delayed response characteristics (Lamontagne *et al.*, 2018; Barros
610 *et al.*, 2018). The observed peak 1~2 years after initial impoundment in Chinese RIS is
611 similar in timescale to the rapid response mode in France, but the decay after the peak
612 may be slower due to the higher regional tectonic stress background and more active
613 faulting. Additionally, for special scenarios like cascade reservoirs, the superposition
614 effect of stress perturbations caused by the impoundment and operation of adjacent
615 reservoirs can significantly elevate the peak pore pressure, far exceeding the
616 perturbation amplitude of a single reservoir (Zhang *et al.*, 2021), increasing the
617 complexity of RIS risk assessment. These comparisons indicate that although pore
618 pressure diffusion is a common thread in many RIS cases, its specific temporal
619 manifestation (rapid or delayed) and spatial extent are modulated by the combined
620 effects of regional fault permeability, hydraulic diffusivity, reservoir operation patterns,
621 and the initial tectonic stress level.

622 The correlation analysis in this study leads to an enlightening conclusion for the
623 paradigm of RIS risk assessment: although a Reservoir Capacity greater than 3.2×10^8
624 m^3 or a Reservoir Major Axis exceeding 15.9 km can serve as practical thresholds for
625 preliminary risk screening during the planning stage, all static or dynamic reservoir
626 attribute parameters show only weak or no correlation with the maximum magnitude



627 (M_{\max}). This finding is highly consistent with observations worldwide (Klose, 2013).
628 For example, the study in Brazil explicitly states that no clear trend is observed between
629 the maximum magnitude and Dam Height, Reservoir Capacity, or Reservoir Area
630 (Barros *et al.*, 2018), and Gupta (2002) compilation of 117 global RIS cases also
631 supports this general rule. This statistically confirms that M_{\max} is primarily controlled
632 by inherent geological factors such as the size of local faults, their pre-existing stress
633 state, and rock strength (Talwani, 1997), while static or dynamic reservoir parameters
634 mainly influence the probability and timing of earthquake triggering by modulating the
635 pore pressure diffusion process, rather than directly controlling the final rupture scale.
636 Consequently, traditional empirical models that over-rely on static reservoir parameters
637 for predicting M_{\max} have clear limitations. Based on this, the future framework for RIS
638 risk assessment should gradually shift beyond static empirical models towards models
639 that integrate multi-source information and physical processes. The W-score model
640 developed in this study, which couples the observed power-law decay of RIS with M_{\max}
641 Distance and its Time Lag since initial impoundment, provides a new quantitative tool
642 for the probabilistic identification of RIS events. This direction aligns with the
643 probabilistic identification framework combining reservoir length, volume, and
644 tectonic background proposed earlier by Grasso *et al.* (2018), and the "pore pressure-
645 fault activity" coupling indicator suggested by Miao *et al.* (2025) for cascade reservoirs,
646 representing a common trend in development. For engineering practice in China, we
647 recommend significantly expanding the monitoring and assessment range from the
648 current 10 km to the 30–40 km permeability boundary identified in this study within



649 the current standards. A dual-threshold screening process based on tectonic activity and
650 reservoir geometric parameters (*e.g.*, Reservoir Capacity or Reservoir Major Axis)
651 should be introduced during the planning stage of reservoir construction. In the long
652 term, it is essential to develop coupled multi-physics models that integrate geological
653 structure, in-situ stress field, fault permeability, and hydrogeological conditions to
654 achieve more accurate risk prediction and management.

655 **8 Conclusions**

656 Addressing the insufficient systematic understanding of Reservoir-Induced Seismicity
657 (RIS) patterns in China, this study integrated a high-resolution national reservoir dataset
658 (CRD) with a unified earthquake catalog spanning over fifty years to establish the first
659 national-scale screening sample covering 1,435 large/medium-sized reservoirs, from
660 which 88 induced-type reservoirs were identified. Through systematic analysis of their
661 spatial distribution, spatiotemporal evolution, sequence parameters, and inducing
662 factors, this study reveals a series of fundamental characteristics and physical
663 mechanisms of RIS in China and offers new insights for risk assessment applications.
664 The main conclusions are as follows:

665 1. RIS spatial distribution is dominated by the regional tectonic background,
666 exhibiting significant selectivity. Induced-type reservoirs are not uniformly distributed
667 but are highly concentrated in strong tectonic activity zones such as the Sichuan-
668 Yunnan rhombic block along the eastern margin of the Tibetan Plateau. Their spatial
669 pattern shows a high degree of coupling with Late Pleistocene active faults and
670 historical moderate-to-strong ($M \geq 4.0$) seismicity. This clearly indicates that high



671 tectonic stress accumulation and developed fault systems are prerequisite geological
672 conditions for RIS occurrence. In contrast, the tectonically stable eastern region, despite
673 having a high density of reservoirs, shows a significantly lower probability of induction.
674 This pattern provides a reference basis for the macro-siting of major hydropower
675 projects.

676 2. RIS spatiotemporal evolution is dominated by the pore pressure diffusion
677 mechanism, with an influence range far exceeding the current standard. RIS events
678 exhibit a significant power-law decay with increasing distance from the reservoir
679 shoreline (M_{\max} Distance), with 95% and 99% of events concentrated within 24.8 km
680 and 38.2 km, respectively. Temporally, seismic activity peaks 1~2 years after
681 impoundment, showing a typical delayed response. The W-score model established
682 based on these characteristics effectively quantifies the spatiotemporal coupling effect,
683 providing a new tool for the probabilistic identification of RIS events. The effective
684 boundary of reservoir water penetration determined in this study (30~40 km) far
685 exceeds the 10 km zone suggested in the current national standard (GB 21075-2007).
686 It is recommended to revise this parameter in future risk assessments to prevent
687 potential underestimation of the spatial risk.

688 3. RIS sequence parameters possess statistical fingerprints distinct from natural
689 earthquakes, revealing a unique triggering and evolution physical process. Compared
690 to natural earthquake sequences, RIS sequences exhibit significantly lower α -values
691 (weaker ability to trigger secondary events) and higher b -values. This reveals that RIS
692 primarily activates critically stressed faults through pore pressure diffusion, leading to



693 unique sequence behavior characterized by a high proportion of small earthquakes and
694 a weaker ability of large earthquakes to trigger secondary sequences. Furthermore, a
695 significant difference emerges between the b -value of RIS sequences and the b -value
696 of background seismicity at a distance of 30~40 km from the shoreline, statistically
697 validating this distance as the critical physical boundary for reservoir water penetration.

698 4. Correlation analysis reveals the fundamental limitations of using static or
699 dynamic reservoir attribute parameters to predict the maximum magnitude, providing
700 crucial evidence for risk assessment. The study finds that a Reservoir Capacity
701 exceeding $3.2 \times 10^8 \text{ m}^3$ or a Reservoir Major Axis exceeding 15.9 km can serve as
702 practical thresholds for preliminary risk screening during the planning stage. However,
703 in-depth correlation matrix analysis shows that both static reservoir attributes (*e.g.*,
704 Reservoir Capacity, Dam Height, Reservoir Area, Capacity / Area, Reservoir Major
705 Axis) and dynamic response parameters (M_{\max} Distance, Time Lag, Peak Lag) have
706 only weak correlations with the RIS maximum magnitude (M_{\max}). This finding
707 statistically confirms that M_{\max} is primarily controlled by geological factors such as
708 local fault development scale, pre-existing stress state, and rock strength, while
709 reservoir parameters mainly influence the probability of earthquake triggering by
710 modulating the pore pressure diffusion process. Therefore, future risk assessment
711 should gradually shift from experience-based models reliant on reservoir scale towards
712 physics-based mechanistic models that integrate geological structure, in-situ stress field,
713 and hydrogeological conditions.

714



715 **Data availability.** The seismic data used in this study were obtained from the *National*
716 *Unified Official Earthquake Catalog* provided by the China Earthquake Networks
717 Center (last accessed on April 15, 2025, via <http://10.5.160.18/console/exit.action>).
718 This catalog contains earthquake parameters for events across China from January 1,
719 1970, to March 27, 2025. This earthquake catalog is proprietary and cannot be released
720 to the public. The spatial distribution and fundamental attributes of reservoirs were
721 primarily sourced from the published China Reservoir Dataset (CRD, [Song et al., 2022](#)).
722 Critical reservoir parameters, such as the initial impoundment time and dam height,
723 were compiled and integrated by the authors from publicly available sources, including
724 the *Encyclopedia of Chinese Rivers and Lakes*, local gazetteers, government reports,
725 and news archives. This integrated reservoir attributes dataset is proprietary to this
726 study and may be available from the corresponding author upon reasonable request.
727 The computer codes used for calculating sequence parameters (α -value, b -value, and p -
728 value) and the W-score model in this study are available from the corresponding author
729 upon reasonable request.

730 **Acknowledgments.** Data support was provided by the National Earth System Science
731 Data Center, National Science & Technology Infrastructure of China
732 (<http://www.geodata.cn>). We are grateful to Senior Engineer Xiaojing Ma of the
733 Guangdong Earthquake Agency and Dr. Xinxin Yin of the Gansu Earthquake Agency
734 for their valuable assistance in providing reservoir attribute information. We also extend
735 our sincere appreciation for their support.

736 **Financial support.** This work was supported by the Special Fund of the Institute of
737 Geophysics, China Earthquake Administration and the program of the China Seismic
738 Experimental Site (Grant No. DQJB24Z04).

739 **Competing Interests.** The authors acknowledge there are no conflicts of interest recorded.

740

741

742

743



744 **References**

- 745 Barros, L. V., Assumpção, M., Ribotta, L. C., Ferreira, V. M., De Carvalho, J. M., Bowen, B. M. D.,
746 and Albuquerque, D. F.: Reservoir-Triggered Seismicity in Brazil: Statistical Characteristics in
747 a Midplate Environment, *Bulletin of the Seismological Society of America*, 108, 3046–3061,
748 <https://doi.org/10.1785/0120170364>, 2018.
- 749 Bi, J. M., Jiang, C. S.: Distribution characteristics of earthquake sequence parameters in North
750 China, *Chinese Journal of Geophysics*, 62, 4300–4312, 2019. (in Chinese)
- 751 Chang, Y., Wang, R., Han, P., Wang, J., Miao, M., Zeng, Z., Wu, W., Jiang, C., Meng, L., Shi, H.,
752 and Hattori, K.: b-Value Evaluation and Applications to Seismic Hazard Assessment, *Entropy*,
753 27, 958, <https://doi.org/10.3390/e27090958>, 2025.
- 754 Cheng, H., Zhang, H., Zhu, B., Sun, Y., Zheng, L., Yang, S., and Shi, Y.: Finite element investigation
755 of the poroelastic effect on the Xinfengjiang Reservoir-triggered earthquake, *Sci. China Earth
756 Sci.*, 55, 1942–1952, <https://doi.org/10.1007/s11430-012-4470-8>, 2012.
- 757 Deng, K., Zhou, S., Wang, R., Robinson, R., Zhao, C., and Cheng, W.: Evidence that the 2008 Mw
758 7.9 Wenchuan Earthquake Could Not Have Been Induced by the Zipingpu Reservoir, *Bulletin
759 of the Seismological Society of America*, 100, 2805–2814,
760 <https://doi.org/10.1785/0120090222>, 2010.
- 761 Dong, S., Li, L., Zhao, L., Shen, X., Wang, W., Huang, H., Peng, B., Xu, X., and Gao, R.: Seismic
762 Evidence for Fluid-Driven Pore Pressure Increase and Its Links With Induced Seismicity in the
763 Xinfengjiang Reservoir, South China, *JGR Solid Earth*, 127, e2021JB023548,
764 <https://doi.org/10.1029/2021JB023548>, 2022.
- 765 Gahalaut, K., Tuan, T. A., and Purnachandra Rao, N.: Rapid and Delayed Earthquake Triggering by
766 the Song Tranh 2 Reservoir, Vietnam, *Bulletin of the Seismological Society of America*, 106,
767 2389–2394, <https://doi.org/10.1785/0120160106>, 2016.
- 768 Ghofrani, H. and Atkinson, G. M.: Activation Rate of Seismicity for Hydraulic Fracture Wells in the
769 Western Canada Sedimentary Basin, *Bulletin of the Seismological Society of America*, 110,
770 2252–2271, <https://doi.org/10.1785/0120200002>, 2020.
- 771 Grasso, J. -R., Karimov, A., Amorese, D., Sue, C., and Voisin, C.: Patterns of Reservoir-Triggered
772 Seismicity in a Low-Seismicity Region of France, *Bulletin of the Seismological Society of*



- 773 America, 108, 2967–2982, <https://doi.org/10.1785/0120180172>, 2018.
- 774 Guo, L. J., 2015. A study on the statistical features of earthquake sequence parameters of the North-
775 South Seismic Belt (Master's thesis). Institute of Geophysics, China Earthquake
776 Administration.
- 777 Gupta, H. K., Rastogi, B. K., and Narain, H.: Common features of the reservoir-associated seismic
778 activities, *Bulletin of the Seismological Society of America*, 62, 481–492,
779 <https://doi.org/10.1785/BSSA0620020481>, 1972.
- 780 Gupta, H. K.: A review of recent studies of triggered earthquakes by artificial water reservoirs with
781 special emphasis on earthquakes in Koyna, India, *Earth-Science Reviews*, 58, 279–310,
782 [https://doi.org/10.1016/S0012-8252\(02\)00063-6](https://doi.org/10.1016/S0012-8252(02)00063-6), 2002.
- 783 Jiang, C. S., Han, L. B., Guo, L. J.,: Parameter characteristics in the early period of three earthquake
784 sequences in the Yutian, Xin Jiang since 2008, *Acta Seismologica Sinica*, 36, 165–174, 2014.
785 (in Chinese)
- 786 Jiang, C. S., Wu, Z. L., Han, L. B., Guo, L. J.,: a. Effect of cutoff magnitude M_c of earthquake
787 catalogues on the early estimation of earthquake sequence parameters with implication for the
788 probabilistic forecast of aftershocks: the 2013 Minxian-Zhangxian, Gansu, $M_s6.6$ earthquake
789 sequence, *Chinese Journal of Geophysics*, 56, 4048–4057, 2013b. (in Chinese)
- 790 Jiang, C. S., Wu, Z. L., Yin, F. L., Guo, L. J., Bi, J. M., Wang, Y. W.,: Stability of early-estimation
791 sequence parameters for continuous forecast of the aftershock rate: A case study of the 2014
792 Ludian, Yunnan $M_s6.5$ earthquake, *Chinese Journal of Geophysics*, 58, 4163–4173, 2015. (in
793 Chinese)
- 794 Jiang, C. S., Zhuang, J. C., Long, F., Han, L. B., Guo, L. J.,: Statistical analysis of ETAS parameters
795 in the early stage of the 2013 Lushan $M_s7.0$ earthquake sequence, *Acta Seismologica Sinica*,
796 35, 661–669, 2013a. (in Chinese)
- 797 Jiang, C., Jiang, C. S., Yin, F. L., Zhang, Y. B., Bi, J. M., Long, F., Si, Z. Y., Yin, X. X.,: A new
798 method for calculating b-value of time sequence based on data-driven (TbDD): A case study
799 of the 2021 Yangbi $M_s6.4$ earthquake sequence in Yunnan, *Chinese Journal of Geophysics*, 64,
800 3126–3134, 2021. (in Chinese)
- 801 Julian, B. R. and Foulger, G. R.: Time-dependent seismic tomography: Time-dependent seismic
802 tomography, *Geophysical Journal International*, 182, 1327–1338,



- 803 <https://doi.org/10.1111/j.1365-246X.2010.04668.x>, 2010.
- 804 Klose, C. D.: Mechanical and statistical evidence of the causality of human-made mass shifts on the
805 Earth's upper crust and the occurrence of earthquakes, *J Seismol*, 17, 109–135,
806 <https://doi.org/10.1007/s10950-012-9321-8>, 2013.
- 807 Lamontagne, M., Rogers, G., Cassidy, J., Tournier, J., and Lawrence, M. S.: A Review of Reservoir
808 Monitoring and Reservoir-Triggered Seismicity in Canada, *Bulletin of the Seismological*
809 *Society of America*, 108, 3062–3079, <https://doi.org/10.1785/0120180009>, 2018.
- 810 Li, L. and Luo, G.: What causes the spatiotemporal patterns of seismicity in the Three Gorges
811 Reservoir area, central China?, *Earth and Planetary Science Letters*, 592, 117618,
812 <https://doi.org/10.1016/j.epsl.2022.117618>, 2022.
- 813 Mesimeri, M., Karakostas, V., Papadimitriou, E., and Tsaklidis, G.: Characteristics of earthquake
814 clusters: Application to western Corinth Gulf (Greece), *Tectonophysics*, 767, 228160,
815 <https://doi.org/10.1016/j.tecto.2019.228160>, 2019.
- 816 Miao, M., Han, P., Yao, M., Wang, R., Zhao, C., Zhao, C., Lu, R., Du, Z., and Chen, X.: Spatial-
817 Temporal Pore Pressure and Stress Evolution Associated With the Impoundment of Two
818 Contiguous Reservoirs in Jinsha River, China and Regional Seismicity, *JGR Solid Earth*, 130,
819 e2025JB031220, <https://doi.org/10.1029/2025JB031220>, 2025.
- 820 Mignan, A., Jiang, C., Zechar, J. D., Wiemer, S., Wu, Z., and Huang, Z.: Completeness of the
821 Mainland China Earthquake Catalog and Implications for the Setup of the China Earthquake
822 Forecast Testing Center, *Bulletin of the Seismological Society of America*, 103, 845–859,
823 <https://doi.org/10.1785/0120120052>, 2013.
- 824 Ogata, Y. and Katsura, K.: Analysis of temporal and spatial heterogeneity of magnitude frequency
825 distribution inferred from earthquake catalogues, *Geophysical Journal International*, 113, 727–
826 738, <https://doi.org/10.1111/j.1365-246X.1993.tb04663.x>, 1993.
- 827 Ogata, Y.: Increased probability of large earthquakes near aftershock regions with relative
828 quiescence, *J. Geophys. Res.*, 106, 8729–8744, <https://doi.org/10.1029/2000JB900400>, 2001.
- 829 Ogata, Y.: Statistical Models for Earthquake Occurrences and Residual Analysis for Point Processes,
830 *Journal of the American Statistical Association*, 83, 9–27,
831 <https://doi.org/10.1080/01621459.1988.10478560>, 1988.
- 832 Pearson, K.: VII. Note on regression and inheritance in the case of two parents, *Proceedings of the*



- 833 Royal Society of London, 58, 240–242, <https://doi.org/10.1098/rspl.1895.0041>, 1895.
- 834 Rajendran, K. and Talwani, P.: The role of elastic, undrained, and drained responses in triggering
835 earthquakes at Monticello Reservoir, South Carolina, *Bulletin of the Seismological Society of*
836 *America*, 82, 1867–1888, <https://doi.org/10.1785/BSSA0820041867>, 1992.
- 837 Rigo, A., Vernant, P., Feigl, K. L., Goula, X., Khazaradze, G., Talaya, J., Morel, L., Nicolas, J.,
838 Baize, S., Chery, J., and Sylvander, M.: Present-day deformation of the Pyrenees revealed by
839 GPS surveying and earthquake focal mechanisms until 2011, *Geophysical Journal International*,
840 201, 947–964, <https://doi.org/10.1093/gji/ggv052>, 2015.
- 841 Simpson, D. W., Leith, W. S., and Scholz, C. H.: Two types of reservoir-induced seismicity, *Bulletin*
842 *of the Seismological Society of America*, 78, 2025–2040,
843 <https://doi.org/10.1785/BSSA0780062025>, 1988.
- 844 Song, C., Fan, C., Zhu, J., Wang, J., Sheng, Y., Liu, K., Chen, T., Zhan, P., Luo, S., Yuan, C., and
845 Ke, L.: A comprehensive geospatial database of nearly 100 000 reservoirs in China, *Earth Syst.*
846 *Sci. Data*, 14, 4017–4034, <https://doi.org/10.5194/essd-14-4017-2022>, 2022.
- 847 Spearman, C.: The Proof and Measurement of Association between Two Things, *The American*
848 *Journal of Psychology*, 15, 72, <https://doi.org/10.2307/1412159>, 1904.
- 849 Talwani, P., Chen, L., and Gahalaut, K.: Seismogenic permeability, k_s , *J. Geophys. Res.*, 112,
850 2006JB004665, <https://doi.org/10.1029/2006JB004665>, 2007.
- 851 Talwani, P.: On the Nature of Reservoir-induced Seismicity, *Pure appl. geophys.*, 150, 473–492,
852 <https://doi.org/10.1007/s000240050089>, 1997.
- 853 Trivedi, P. C.: Application of Omori's Decay Law to the 2001 Bhuj Aftershock Sequence for
854 Kachchh Region of Western India, *OJER*, 04, 94–101, <https://doi.org/10.4236/ojer.2015.43009>,
855 2015.
- 856 Utsu, T.: Representation and Analysis of the Earthquake Size Distribution: A Historical Review and
857 Some New Approaches, *Pure appl. geophys.*, 155, 509–535,
858 <https://doi.org/10.1007/s000240050276>, 1999.
- 859 Wang, J.-H.: On the correlation of observed Gutenberg-Richter's b value and Omori's p value for
860 aftershocks, *Bulletin of the Seismological Society of America*, 84, 2008–2011,
861 <https://doi.org/10.1785/BSSA0840062008>, 1994.
- 862 Wang, Y. W., Jiang, C. S., Liu, F., Bi, J. M.: Assessment of earthquake monitoring capability and



863 score of seismic station detection capability in China Seismic Network (2008-2015)., Chinese
864 Journal of Geophysics, 60, 2767–2778, 2017. (in Chinese)

865 Xue, Y., Xie, M. Y., Liu, J., Zhuang J. C.: Study on foreshock sequences of the global great shallow-
866 focus earthquakes with $MW \geq 8.0$, Seismology and Geology, 43, 1233–1249, 2021. (in Chinese)

867 Yin, F. and Jiang, C.: Enhanced b -value time-series calculation method using data-driven approach,
868 Geophysical Journal International, 236, 78–87, <https://doi.org/10.1093/gji/ggad419>, 2023.

869 Zaliapin, I., Gabrielov, A., Keilis-Borok, V., and Wong, H.: Clustering Analysis of Seismicity and
870 Aftershock Identification, Phys. Rev. Lett., 101, 018501,
871 <https://doi.org/10.1103/PhysRevLett.101.018501>, 2008.

872 Zhang, M., Ge, S., Yang, Q., and Ma, X.: Impoundment-Associated Hydro-Mechanical Changes
873 and Regional Seismicity Near the Xiluodu Reservoir, Southwestern China, JGR Solid Earth,
874 126, e2020JB021590, <https://doi.org/10.1029/2020JB021590>, 2021.

875 Zhuang, J., Ogata, Y., and Vere-Jones, D.: Stochastic Declustering of Space-Time Earthquake
876 Occurrences, Journal of the American Statistical Association, 97, 369–380,
877 <https://doi.org/10.1198/016214502760046925>, 2002.

878



879 **Figure Captions**

880 **Table 1.** Inventory of 88 identified induced-reservoirs in China with reservoir properties and

881 parameters of the largest induced earthquake (M_{\max}).

882

883 **Table 2.** Statistical parameters (α -value, p -value and b -value) of natural tectonic earthquake

884 sequences.

885

886 **Figure 1.** Example of identified reservoir-induced seismicity sequences at the Jinping-I Reservoir.

887 (a) Reservoir boundary and spatial distribution of seismicity. Gray dots represent background

888 seismicity recorded from 1970 to the initial impoundment; red dots represent earthquakes after the

889 initial impoundment; purple dashed lines outline the spatiotemporal clusters of induced sequences;

890 black curves denote active faults since the Late Pleistocene; gradient green areas indicate zones

891 within 10, 20, 30, 40, and 50 km from the reservoir shoreline. The inset shows the location of the

892 study area. (b) Normalized frequency distribution of induced earthquakes as a function of distance

893 from the reservoir shoreline (for the 0–20 km range, with 1 km bins). Subplots (from top to

894 bottom) show results for completeness magnitudes (M_C) of M_L 2.0, 2.5, and 3.0, respectively. (c)

895 Temporal comparison of cumulative earthquake frequency (from one year before to ten years after

896 the initial impoundment). "Inside" denotes the induced sequence within the reservoir area,

897 "outside" denotes background seismicity outside the reservoir area, and "all" denotes all

898 earthquakes. Curves are normalized to their maximum values. The green vertical dashed line

899 marks the time of initial impoundment. Subplots (from top to bottom) correspond to (M_C) of M_L

900 2.0, 2.5, and 3.0, respectively.



901

902 **Figure 2.** Spatial distribution characteristics of reservoir-induced seismicity in China. (a) Spatial
903 distribution of large/medium-sized reservoirs and reservoirs with induced seismicity. Blue
904 polygons represent large/medium-sized reservoirs (capacity $\geq 1 \times 10^8$ m³) with complete
905 parameters (*e.g.*, impoundment time, dam height); red polygons represent reservoirs with induced
906 seismicity, identified based on spatiotemporal clustering. (b) Spatial density of reservoirs with
907 induced seismicity (units: number per square degree). (c) Spatial distribution of the proportion of
908 reservoirs with induced seismicity among all large/medium-sized reservoirs. (d) Density
909 distribution of $M \geq 4.0$ earthquakes in China (units: number per square degree) and mapped active
910 faults (brown lines).

911

912 **Figure 3.** Spatiotemporal patterns of reservoir-induced seismicity and construction of the W-score
913 table. (a) Empirical distribution of normalized earthquake frequency versus distance from the
914 reservoir shoreline, with the blue curve showing the fit of a power-law function. (b) Empirical
915 distribution of normalized earthquake frequency versus time lag since initial impoundment, with
916 the red curve showing the fit of an exponential-linear hybrid model. (c) W-score table constructed
917 based on the joint distribution of reservoir distance and time lag. The color fill indicates the
918 probability of induced seismicity; black contour lines mark the boundaries for probabilities of 0.2,
919 0.3, 0.5, and 0.9. (d) Example application of the W-score table, using the Jinping-I Reservoir and
920 induced seismicity identification results for a completeness magnitude $M_C = M_L 2.5$. Circles
921 represent manually identified induced earthquakes, squares represent background earthquakes, and
922 the color fill indicates the probability of induced seismicity.



923

924 **Figure 4.** Parameter characteristics of the reservoir-induced seismicity sequences. (a) Statistical
925 distribution of the α -value from the ETAS model for the induced sequences. (b) Statistical
926 distribution of the p -value from the ETAS model. (c) Statistical distribution of the b -value
927 estimated using the OK1993 model. (d) Scatter plot of α -value versus b -value. (e) Scatter plot of
928 p -value versus b -value. (f) Scatter plot of α -value versus p -value. In panels (d) to (f), the blue
929 contours represent the bivariate kernel density estimate (KDE) for parameters of natural tectonic
930 seismicity sequences from previous studies, and the red contours represent the KDE for
931 parameters of the induced seismicity sequences from this study.

932

933 **Figure 5.** Statistical characteristics of the Kolmogorov-Smirnov (KS) test comparing the b -values
934 of induced sequences and background seismicity. (a) Zonal KS test results: b -values of
935 background seismicity within concentric distance zones (0~10, 10~20, 20~30, 30~40, 40~50 km
936 from the reservoir shoreline) are compared against the b -value of the induced sequence. The KS
937 statistic (D) and significance level (P) are plotted against distance. (b) Cumulative zonal KS test
938 results: based on b -values of background seismicity within cumulative distance ranges (0~10,
939 0~20, 0~30, 0~40, 0~50 km). The red horizontal dashed lines in both panels indicate the statistical
940 significance threshold ($P = 0.05$).

941

942 **Figure 6.** Correlation analysis between the maximum magnitude (M_{\max}) of induced seismicity and
943 potential inducing factors. (a) Reservoir capacity (Reservoir Capacity, 10^8 m³). (b) Dam height
944 (Dam Height, m). (c) Reservoir surface area (Reservoir Area, km²). (d) Mean water depth (Capacity



945 / Area, m). (e) Reservoir major axis length (Reservoir Major Axis, km). (f) Distance from the
946 reservoir shoreline of the M_{\max} event (M_{\max} Distance, km). (g) Time lag of the M_{\max} event since
947 initial impoundment (Time Lag, days). (h) Time lag of the peak seismicity rate since initial
948 impoundment (Peak Lag, days). The Pearson correlation coefficient (r), Spearman correlation
949 coefficient (ρ), and the corresponding significance level (P) are indicated textually in each subplot.
950

951 **Figure 7.** Proportion characteristics of induced-type reservoirs under the influence of single factors.

952 (a) Proportion across different bins of dam height (Dam Height, m). (b) Proportion across different
953 bins of reservoir capacity (Reservoir Capacity, 10^8 m³). (c) Proportion across different bins of
954 reservoir major axis length (Reservoir Major Axis, km). (d) Proportion across different bins of mean
955 water depth (Capacity / Area, m). (e) Proportion across different bins of reservoir surface area
956 (Reservoir Area, km²). In each subplot, the purple filled area represents the proportion of induced-
957 type reservoirs for the respective bin, and the gray filled area represents the proportion of non-
958 induced-type reservoirs.

959

960 **Figure 8.** Pearson correlation matrix among inducing factors. The lower triangle of the matrix

961 visualizes the correlation coefficients using ellipses: flatter ellipses indicate stronger correlations; a
962 45° tilt indicates a positive correlation, and a -45° tilt indicates a negative correlation; asterisks
963 indicate the statistical significance level (* $P < 0.05$, ** $P < 0.01$). The upper triangle displays the
964 Pearson correlation coefficient (r) numerically, with colors transitioning from blue (strong negative
965 correlation) through green (weak correlation) to yellow (strong positive correlation). The inducing
966 factors are: Reservoir Capacity (10^8 m³), Dam Height (m), Reservoir Area (km²), Capacity / Area



967 (m), Reservoir Major Axis (km), M_{\max} Distance (km), Time Lag (days), Peak Lag (days).

968

969 **Figure 9.** Spearman correlation matrix among inducing factors. In the lower triangle of the matrix,

970 ellipses visualize the rank correlation coefficients: flatter ellipses indicate stronger correlations; a

971 45° tilt indicates a positive correlation, and a -45° tilt indicates a negative correlation; asterisks

972 indicate the statistical significance level (* $P < 0.05$, ** $P < 0.01$). The upper triangle displays the

973 Spearman correlation coefficient (ρ) numerically, with colors transitioning from blue (strong

974 negative correlation) through green (weak correlation) to yellow (strong positive correlation). The

975 inducing factors are the same as in [Figure 8](#).

976

977



Table 1. Inventory of 88 identified induced-reservoirs in China with reservoir properties and parameters of the largest induced earthquake (M_{max}).

No.	Reservoir Name	Initial Impoundment Date	Reservoir Capacity (10^8 m^3)	Reservoir Area (km^2)	Dam Height (m)	Major Axis (km)	Capacity/Area (m)	M_{max} Distance (km)	Time Lag (days)	Peak Lag (days)	M_{max} Event Details			
											Date	Date	Mag.	Lat. ($^{\circ}\text{N}$)
1	Dali	1975/08/30	0.117	1.36	62.00	1.85	8.60	17.20	17918	470	2024/09/18	4.8	31.97	117.50
2	Yinpan	2011/04/30	3.200	11.24	80.00	11.02	109.00	6.27	2400	3376	2017/11/23	5.0	29.39	107.99
3	Shuikou	1993/03/31	23.400	100.27	101.00	66.90	23.30	0.27	5455	9724	2008/03/06	4.2	26.37	118.67
4	Admiralty	2010/05/30	1.060	3.16	97.50	5.86	33.50	1.11	1193	642	2013/09/04	4.8	25.64	118.75
5	Haidianxia	2005/12/13	0.298	3.19	46.00	11.71	9.30	0.93	1402	4200	2009/10/15	3.9	35.02	103.79
6	Jiudianxia	2007/12/01	10.040	24.06	136.00	29.47	41.70	0.65	508	2647	2009/04/22	3.4	34.82	103.81
7	Jiefangcun	1971/08/30	0.606	6.09	16.00	3.86	10.00	9.25	14244	14248	2010/08/29	2.8	39.91	98.95
8	Xiaoxia	2004/09/30	0.480	18.40	50.70	46.66	2.60	4.11	5951	50	2021/01/14	4.0	36.06	104.07
9	Chaiji Xia	2007/07/30	0.166	3.17	33.00	7.70	5.20	5.06	5436	14200	2022/06/16	3.7	36.21	103.47
10	Daxia	1996/11/30	0.900	6.18	70.00	23.20	14.60	13.86	8812	3938	2021/01/14	4.0	36.06	104.07
11	Bikou	1976/01/01	5.210	13.94	101.80	23.31	37.40	12.31	11872	11873	2008/07/03	4.0	32.70	105.00



No.	Reservoir Name	Initial Impoundment Date	Reservoir Capacity (10^8 m^3)	Reservoir Area (km^2)	Dam Height (m)	Major Axis (km)	Capacity/Area (m)	M_{max} Distance (km)	Time Lag (days)	Peak Lag (days)	M_{max} Event Details			
											Date	Date	Mag.	
12	Zhaizhaizi	1989/10/30	0.120	1.39	25.00	1.35	8.60	2.66	5937	2185	2006/01/30	3.0	38.43	100.95
13	Longshou II	2002/04/30	0.177	1.99	146.50	5.50	8.90	12.64	525	752	2003/10/06	4.2	38.82	100.02
14	Shuangshusi	1975/05/30	0.111	1.30	58.50	3.73	8.50	10.83	10376	10376	2003/10/25	6.1	38.35	100.93
15	Jinjiang	1973/07/01	4.180	20.18	63.20	12.23	20.70	19.81	18389	2357	2023/11/04	4.9	22.09	112.24
16	Fengzishan	1977/01/01	0.149	1.69	93.00	3.18	8.80	13.56	17109	17109	2023/11/04	4.9	22.09	112.24
17	Yangjiang Nuclear	2005/06/30	0.118	1.37	101.00	3.20	8.60	0.06	1835	1835	2010/07/09	3.9	21.74	112.30
18	Jintan	2008/01/01	2.490	7.57	123.30	8.07	32.90	6.62	3205	3203	2016/10/10	2.8	24.52	113.10
19	Hengxi	1978/07/30	0.312	3.33	82.00	4.71	9.40	6.21	15495	15469	2020/12/31	3.4	25.03	113.16
20	Dahua	1982/05/01	9.640	13.01	78.50	33.50	74.10	5.72	3938	233	1993/02/10	4.9	23.63	107.88
21	Yantan	1992/03/01	33.500	126.86	110.00	110.58	26.40	5.96	11168	5609	2022/09/28	4.3	24.34	107.46
22	Longtan	2006/09/30	273.000	372.08	216.50	178.12	73.40	0.00	6348	194	2024/02/15	4.3	25.20	106.73



No.	Reservoir Name	Initial Impoundment Date	Reservoir Capacity (10^8 m^3)	Reservoir Area (km^2)	Dam Height (m)	Major Axis (km)	Capacity/Area (m)	M_{\max} Distance (km)	Time Lag (days)	Peak Lag (days)	M_{\max} Event Details			
											Date	Mag.	Lat. (°N)	Lon. (°E)
23	Letan	2006/01/07	9.500	32.66	80.00	49.67	29.10	4.63	4223	6188	2017/07/31	4.2	23.93	108.60
24	Jinjian	2009/04/05	2.309	5.75	42.70	21.35	40.20	15.90	2659	7959	2016/07/16	3.4	23.43	107.49
25	Guangzhao	2007/12/30	32.450	47.83	200.50	33.00	67.90	8.74	279	717	2008/10/04	4.0	26.00	105.35
26	Huanghuazhai	2010/10/18	1.630	3.95	110.00	13.65	41.30	30.24	5001	5001	2024/06/27	4.1	25.44	106.55
27	Shannipo	2014/11/26	0.850	3.28	119.40	13.55	25.90	4.77	3528	1015	2024/07/24	4.5	26.27	104.74
28	Sanbanxi	2006/01/01	40.940	80.18	185.50	54.63	51.10	0.45	3375	3985	2015/03/30	5.5	26.58	108.84
29	Tianshengqiao II	1992/12/30	0.121	1.40	178.00	13.60	8.60	2.86	2783	1535	2000/08/13	3.9	24.92	105.12
30	Tianshengqiao I	1998/08/01	108.000	174.65	178.00	84.64	61.80	0.75	67	3998	1998/10/06	4.0	24.65	104.85
31	Dongqing	2009/08/20	9.550	23.37	150.00	27.96	40.90	1.97	411	573	2010/10/04	4.3	25.51	105.75
32	Shatuo	2013/04/20	9.100	23.78	116.50	62.45	38.30	0.00	2357	5024	2019/10/02	4.7	28.42	108.38
33	Goupitan	2008/11/29	64.510	87.53	232.50	72.56	73.70	0.91	4570	5455	2021/06/04	3.6	27.42	107.48
34	Dalong	2006/09/30	4.680	14.34	65.50	17.20	32.60	4.16	4708	13163	2019/08/20	4.0	18.52	109.40



No.	Reservoir Name	Initial Impoundment Date	Reservoir Capacity (10^8 m^3)	Reservoir Area (km^2)	Dam Height (m)	Major Axis (km)	Capacity/Area (m)	M_{\max} Distance (km)	Time Lag (days)	Peak Lag (days)	M_{\max} Event Details			
											Date	Mag.	Lat. (°N)	Lon. (°E)
35	Baicaoping	1974/01/01	0.465	2.07	42.00	2.77	22.50	5.30	14399	14388	2013/06/03	3.2	37.63	114.27
36	Pingwang	1977/12/30	0.304	3.24	23.50	3.56	9.40	5.83	2086	952	1983/09/15	4.1	37.52	114.27
37	Xiaolangdi	1999/09/30	126.500	235.35	154.00	70.89	53.70	0.00	1347	605	2003/06/08	3.6	35.08	111.93
38	Gaoguan	1973/12/30	2.120	13.13	45.60	9.58	16.10	23.85	11990	11990	2006/10/27	4.2	31.48	113.08
39	Xiaka River	1980/01/01	0.259	1.53	28.50	4.13	16.90	2.23	10714	10714	2009/05/01	3.2	31.46	112.24
40	Longyu Lake	1975/04/30	0.248	2.70	16.00	5.59	9.20	9.53	12421	12421	2009/05/01	3.2	31.46	112.24
41	Geheyan	1993/04/10	34.000	73.12	151.00	77.95	46.50	7.69	51	910	1993/05/30	3.3	30.32	110.97
42	Xuanniaoguan	2005/04/30	0.129	1.48	65.50	4.13	8.70	2.42	6626	548	2023/06/21	3.3	31.30	111.31
43	Tianfumiao	1978/01/12	0.625	2.40	62.30	7.00	26.00	5.17	16596	7670	2023/06/21	3.3	31.30	111.31
44	Three Gorges	2003/06/01	393.000	894.20	181.00	450.21	44.00	5.25	3852	5907	2013/12/16	5.1	31.10	110.45
45	Mengquan	1981/01/01	0.511	5.56	43.00	5.68	9.20	4.42	9362	11436	2006/08/19	3.6	29.37	111.33
46	Dongjiang	1986/07/31	92.700	168.88	157.00	40.50	54.90	28.56	10936	5014	2016/07/08	4.1	25.90	113.05



No.	Reservoir Name	Initial Impoundment Date	Reservoir Capacity (10^8 m^3)	Reservoir Area (km^2)	Dam Height (m)	Major Axis (km)	Capacity/Area (m)	M_{max} Distance (km)	Time Lag (days)	Peak Lag (days)	M_{max} Event Details			
											Date	Mag.	Lat. (°N)	Lon. (°E)
47	Wannipo	2003/11/30	3.780	10.01	64.50	15.27	37.80	10.55	4631	355	2016/08/03	3.3	28.72	109.37
48	Yihe Nuocer	1987/10/30	1.664	15.33	4.70	7.16	10.90	18.31	6945	17918	2006/11/03	4.2	43.55	119.68
49	Shankouyan	2012/06/21	1.050	3.90	99.10	6.54	26.90	11.91	1842	4591	2017/07/06	2.9	27.60	113.91
50	Baishan	1982/11/16	62.200	139.88	149.50	81.33	44.50	8.31	9760	3698	2009/08/05	4.2	42.27	127.19
51	Biliute	1983/08/26	9.340	56.86	53.30	21.53	16.40	0.00	5281	1101	1998/02/08	4.2	39.92	122.48
52	Sherwo	1972/11/30	7.910	37.18	50.30	18.16	21.30	2.31	753	5217	1974/12/22	5.2	41.20	123.60
53	Bando	2010/10/23	0.150	1.46	78.72	7.20	10.30	0.20	2185	3622	2016/10/16	2.9	35.30	100.27
54	Modo	2009/12/30	1.186	5.00	73.00	8.08	23.70	11.69	2482	27	2016/10/16	2.9	35.30	100.27
55	Xiaogangou	1991/11/30	0.110	0.77	55.00	4.68	14.30	10.22	10554	1440	2020/10/21	3.0	35.92	94.84
56	Hot Spring	1993/08/30	2.550	43.99	17.50	15.56	5.80	0.00	4595	752	2006/03/30	3.5	35.73	95.37
57	Dangka	2015/01/15	0.154	1.74	32.60	5.73	8.90	2.53	2689	5436	2022/05/26	4.1	32.56	96.61
58	Jiangkou	1992/05/12	2.770	22.97	50.70	33.09	12.10	6.33	7616	466	2013/03/18	3.3	31.61	107.76



No.	Reservoir Name	Initial Impoundment Date	Reservoir Capacity (10^8 m^3)	Reservoir Area (km^2)	Dam Height (m)	Major Axis (km)	Capacity/Area (m)	M_{max} Distance (km)	Time Lag (days)	Peak Lag (days)	M_{max} Event Details			
											Date	Mag.	Lat. (°N)	Lon. (°E)
59	Yangjiaba	1999/06/30	0.144	1.64	53.40	4.54	8.80	9.77	7795	7726	2020/10/31	4.0	32.10	105.17
60	Gongzui	1979/01/01	3.570	17.37	85.60	27.63	20.60	7.92	13163	1420	2015/01/14	5.0	29.30	103.20
61	Jinping I	2012/11/30	77.600	85.88	305.00	70.67	90.40	0.70	1486	1320	2016/12/25	4.3	27.89	101.38
62	Buscy	2010/09/28	0.694	6.90	140.80	11.35	10.10	7.74	641	2783	2012/06/30	3.9	28.13	101.18
63	Guandi	2011/10/30	7.597	18.39	168.00	40.18	41.30	13.11	233	408	2012/06/19	3.3	28.24	101.72
64	Guanyinyan	2010/07/01	22.500	45.38	159.00	71.64	49.60	17.38	3837	9618	2021/01/01	3.5	26.21	101.24
65	Ertan	1985/04/30	58.000	98.65	240.00	90.26	58.80	6.55	3985	744	1996/03/28	3.7	27.35	101.88
66	Qiaoqi	2006/12/05	2.120	4.15	123.00	4.24	51.10	5.49	1187	3863	2010/03/05	3.5	30.78	102.75
67	Xiangjiaba	2012/10/10	51.630	99.57	161.00	85.55	51.90	23.10	676	4867	2014/08/17	5.2	28.12	103.51
68	Mangcuo Lake	1980/01/01	2.700	21.77	30.00	8.11	12.40	3.68	14227	2014	2018/12/13	4.9	29.60	98.84
69	Awoduo	2005/10/10	0.147	1.67	53.20	2.49	8.80	2.69	5225	2689	2020/01/30	4.5	28.66	91.97
70	Sujiahekou	2010/04/05	2.230	5.67	131.49	13.54	39.30	8.23	3663	3663	2020/04/15	3.7	25.26	98.30



No.	Reservoir Name	Initial Impoundment Date	Reservoir Capacity (10 ⁸ m ³)	Reservoir Area (km ²)	Dam Height (m)	Major Axis (km)	Capacity/Area (m)	M_{max} Distance (km)	Time Lag (days)	Peak Lag (days)	M_{max} Event Details			
											Date	Mag.	Lat. (°N)	Lon. (°E)
71	Xiaowan	2008/12/16	150.000	196.66	292.00	124.62	76.30	11.87	2510	3683	2015/10/30	5.0	25.04	99.44
72	Qinghai Lake	2011/05/17	0.654	6.53	6.70	5.09	10.00	4.78	927	6945	2013/11/28	4.7	25.40	100.58
73	Gongguoqiao	2011/09/21	3.160	13.28	105.00	35.06	23.80	4.88	2068	927	2017/05/20	4.1	25.66	99.34
74	Longjiang	2010/03/01	12.170	32.59	110.00	35.46	37.30	0.11	5255	2274	2024/07/19	4.5	24.30	98.10
75	Liyuan	2014/11/10	7.270	16.14	155.00	44.49	45.00	5.98	353	7586	2015/10/29	4.8	27.55	100.30
76	Madushan	2010/12/01	5.510	21.53	105.50	50.16	25.60	0.00	2151	1572	2016/10/21	3.0	23.20	102.91
77	Yunpeng	2006/12/03	1.407	13.16	104.00	38.28	10.70	7.82	3897	18389	2017/08/04	3.9	24.20	103.65
78	Rudila	2013/04/30	17.183	64.32	140.00	55.29	26.70	2.21	2274	676	2019/07/21	4.9	26.15	100.55
79	Ahai	2011/12/11	8.280	24.09	138.00	54.27	34.40	3.84	1382	645	2015/09/22	3.7	27.69	100.29
80	Nuozhadu	2013/10/17	237.000	299.76	261.50	117.15	79.10	1.69	3995	6348	2024/09/23	4.0	23.37	100.06
81	Ma'anshan	1984/01/01	0.134	1.53	16.60	2.28	8.80	20.47	14399	9814	2023/06/03	2.9	22.86	104.58
82	Leidatan	2006/02/03	0.940	6.04	84.00	24.26	15.60	2.47	4200	256	2017/08/04	3.9	24.20	103.65



Reservoir No.	Reservoir Name	Initial Impoundment		Reservoir		Dam		Major Capacity/Area		M_{max}		M_{max} Event Details		
		Capacity (10^8 m^3)	Area (km^2)	Height (m)	Axis (km)	Capacity (m)	Distance (km)	Time Lag (days)	Peak Lag (days)	Date	Mag.	Lat. ($^{\circ}\text{N}$)	Lon. ($^{\circ}\text{E}$)	
83	Xiluodu	126.700	127.99	285.50	137.88	99.00	2.25	470	14227	2014/08/17	5.2	28.12	103.51	
84	Jiaokou	1.200	4.59	66.00	6.00	26.10	2.06	7799	13283	1994/09/07	4.7	29.82	121.25	
85	Lubu	0.263	1.69	34.00	2.56	15.60	14.80	3934	9419	1994/09/07	4.7	29.82	121.25	
86	Lishimen	1.990	7.47	74.30	8.77	26.60	4.28	14200	4708	2017/02/13	4.0	29.09	120.68	
87	Shanxi	18.240	40.79	132.00	25.76	44.70	0.00	1865	3852	2006/02/09	4.6	27.68	120.00	
88	Lanxiqiao	0.140	1.07	78.00	3.08	13.10	5.26	4958	4958	1998/02/24	3.6	27.58	119.13	



982 **Table 2.** Statistical parameters (α -value, p -value and b -value) of natural tectonic earthquake
 983 sequences.

No.	α -value	p -value	b -value	Location of Earthquake Sequence	Reference
1	2.2611	0.9312	0.9889	North China, China	Bi and Jiang (2019)
2	1.9171	1.0576	1.0124	North China, China	Bi and Jiang (2019)
3	1.3486	0.7801	0.7797	North China, China	Bi and Jiang (2019)
4	1.5605	1.1545	0.9087	North China, China	Bi and Jiang (2019)
5	2.0487	0.9736	0.5000	North China, China	Bi and Jiang (2019)
6	1.2415	0.7789	0.8300	North China, China	Bi and Jiang (2019)
7	1.6860	1.1985	0.8069	North China, China	Bi and Jiang (2019)
8	1.5212	1.1230	0.7338	North China, China	Bi and Jiang (2019)
9	1.7802	0.8583	0.8823	North China, China	Bi and Jiang (2019)
10	1.5136	0.7757	1.0592	North China, China	Bi and Jiang (2019)
11	2.3568	1.0973	0.5758	North China, China	Bi and Jiang (2019)
12	1.6481	0.9321	0.7192	North China, China	Bi and Jiang (2019)
13	2.0762	1.1156	1.0906	North China, China	Bi and Jiang (2019)
14	2.0091	1.0333	0.9240	North China, China	Bi and Jiang (2019)
15	1.6155	0.9355	0.7081	North China, China	Bi and Jiang (2019)
16	1.2621	0.8847	0.7795	North China, China	Bi and Jiang (2019)
17	1.8200	2.0250	1.0700	Western Corinth Gulf, Greece	Mesimeri <i>et al.</i> (2019)
18	0.7890	2.1360	0.7000	Western Corinth Gulf, Greece	Mesimeri <i>et al.</i> (2019)
19	0.9710	1.5610	0.9200	Western Corinth Gulf, Greece	Mesimeri <i>et al.</i> (2019)



No.	α -value	p -value	b -value	Location of Earthquake Sequence	Reference
20	1.3580	1.4570	0.9000	Western Corinth Gulf, Greece	Mesimeri et al. (2019)
21	1.8900	1.2200	0.7200	Lushan, Sichuan, China	Jiang et al. (2013b)
22	1.7200	1.1485	/	Min County - Zhang County, Gansu, China	Jiang et al. (2013a)
23	1.6820	0.6692	/	Yutian, Xinjiang, China	Jiang et al. (2014)
24	1.8347	1.5569	0.7821	Kuril Islands, Russia	Xue et al. (2021)
25	1.9296	1.7326	0.8220	Kuril Islands, Russia	Xue et al. (2021)
26	2.2996	1.4557	1.1394	Kuril Islands, Russia	Xue et al. (2021)
27	2.1400	1.3663	0.7491	Off the coast of Honshu, Japan	Xue et al. (2021)
28	1.3439	1.2878	1.2818	Off the coast of Honshu, Japan	Xue et al. (2021)
29	1.5563	0.9113	0.7625	Santa Cruz Islands, Solomon Islands	Xue et al. (2021)
30	1.4872	1.7976	0.9349	Santa Cruz Islands, Solomon Islands	Xue et al. (2021)
31	2.0001	1.6973	0.8132	Off the coast of northern, Chile	Xue et al. (2021)
32	2.0970	1.4571	0.8833	Off the coast of northern, Chile	Xue et al. (2021)
33	1.0832	1.5272	0.9723	Off the coast of northern, Chile	Xue et al. (2021)
34	1.5193	0.6645	/	Ludian, Yunnan, China	Guo (2015)
35	1.6165	0.9586	/	Muli, Sichuan, China	Guo (2015)
36	1.9082	0.9281	/	Northeast of Mengzi, Yunnan, China	Guo (2015)
37	1.4829	0.8193	/	Northwest of Yingjiang, Yunnan, China	Guo (2015)
38	2.1897	1.0510	/	Northwest of Garzê, Sichuan, China	Guo (2015)
39	1.1823	1.1546	/	Jianchuan, Yunnan, China	Guo (2015)
40	1.8641	1.1987	/	North of Menyuan, Qinghai, China	Guo (2015)



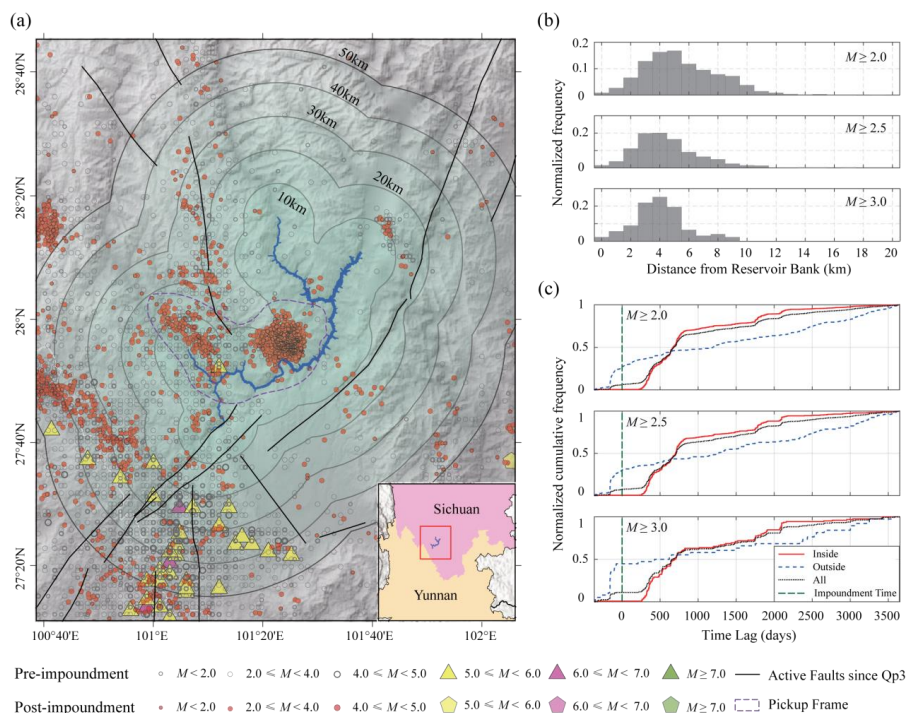
No.	α -value	p -value	b -value	Location of Earthquake Sequence	Reference
41	4.1992	1.0944	/	Southwest of Zhongba, Tibet, China	Guo (2015)
42	1.2166	1.1223	/	Gonghe, Qinghai, China	Guo (2015)
43	2.3933	1.0757	/	Shidian, Yunnan, China	Guo (2015)
44	2.7122	1.0713	/	Dayao, Yunnan, China	Guo (2015)
45	3.9338	1.0077	/	Minle and Shandan, Gansu, China	Guo (2015)
46	5.2438	1.2607	/	Baoshan, Yunnan, China	Guo (2015)
47	2.2892	0.8905	/	Barkam, Sichuan, China	Guo (2015)
48	1.0478	1.0135	/	Baoshan, Yunnan, China	Guo (2015)
49	2.0710	1.2727	/	Huize, Sichuan, China	Guo (2015)
50	2.3146	1.0056	/	Myanmar	Guo (2015)
51	2.6223	1.2559	/	Yangbi, Yunnan, China	Guo (2015)
52	2.5879	1.1229	/	Wenchuan, Sichuan, China	Guo (2015)
53	1.4512	0.9181	/	Yingjiang, Yunnan, China	Guo (2015)
54	5.5711	1.4384	/	Eryuan, Yunnan, China	Guo (2015)
55	1.6950	0.9745	/	Yingjiang, Yunnan, China	Guo (2015)
56	2.3327	1.1857	/	Tengchong, Yunnan, China	Guo (2015)
57	2.2742	2.4711	/	Jinta, Gansu, China	Guo (2015)
58	2.5679	1.4200	/	Ninglang, Yunnan, China	Guo (2015)
59	1.2109	0.9480	/	Yiliang, Yunnan, China	Guo (2015)
60	2.8933	1.2979	/	Baiyu, Sichuan, China	Guo (2015)
61	1.5728	1.0687	/	Eryuan, Yunnan, China	Guo (2015)



No.	α -value	p -value	b -value	Location of Earthquake Sequence	Reference
62	2.0009	1.1667	/	Lushan, Sichuan, China	Guo (2015)
63	0.7704	1.1339	/	Changning, Sichuan, China	Guo (2015)
64	3.7824	1.0544	/	Min County, Gansu, China	Guo (2015)
65	2.3201	1.0142	/	Li County, Sichuan, China	Guo (2015)
66	2.1599	0.9962	/	Zuogong, Tibet, China	Guo (2015)

984

985



986

987

988 **Figure 1.** Example of identified reservoir-induced seismicity sequences at the Jinping-I Reservoir.

989 (a) Reservoir boundary and spatial distribution of seismicity. Gray dots represent background

990 seismicity recorded from 1970 to the initial impoundment; red dots represent earthquakes after the

991 initial impoundment; purple dashed lines outline the spatiotemporal clusters of induced sequences;

992 black curves denote active faults since the Late Pleistocene; gradient green areas indicate zones

993 within 10, 20, 30, 40, and 50 km from the reservoir shoreline. The inset shows the location of the

994 study area. (b) Normalized frequency distribution of induced earthquakes as a function of distance

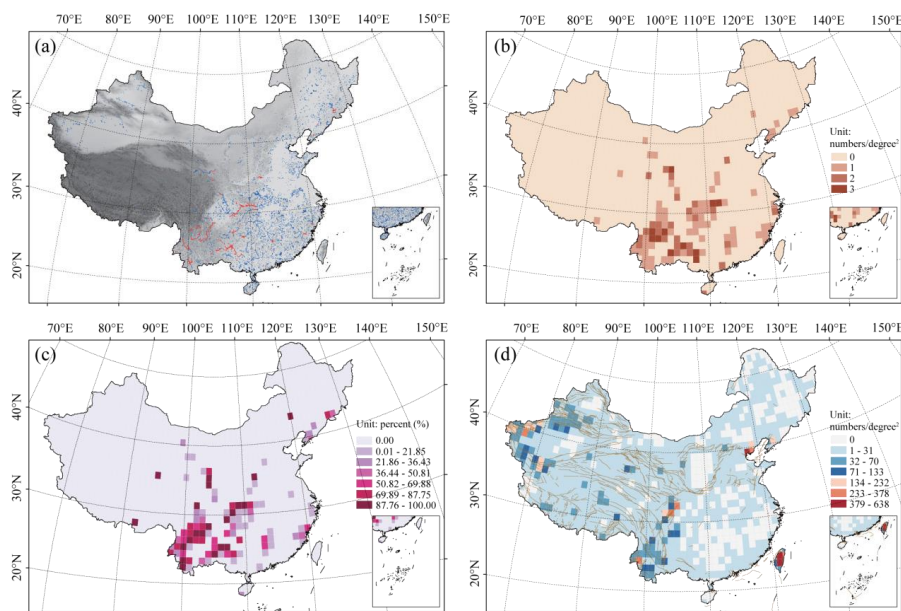
995 from the reservoir shoreline (for the 0~20 km range, with 1 km bins). Subplots (from top to

996 bottom) show results for completeness magnitudes (M_C) of M_L 2.0, 2.5, and 3.0, respectively. (c)

997 Temporal comparison of cumulative earthquake frequency (from one year before to ten years after



998 the initial impoundment). "Inside" denotes the induced sequence within the reservoir area,
999 "outside" denotes background seismicity outside the reservoir area, and "all" denotes all
1000 earthquakes. Curves are normalized to their maximum values. The green vertical dashed line
1001 marks the time of initial impoundment. Subplots (from top to bottom) correspond to (M_C) of M_L
1002 2.0, 2.5, and 3.0, respectively.
1003



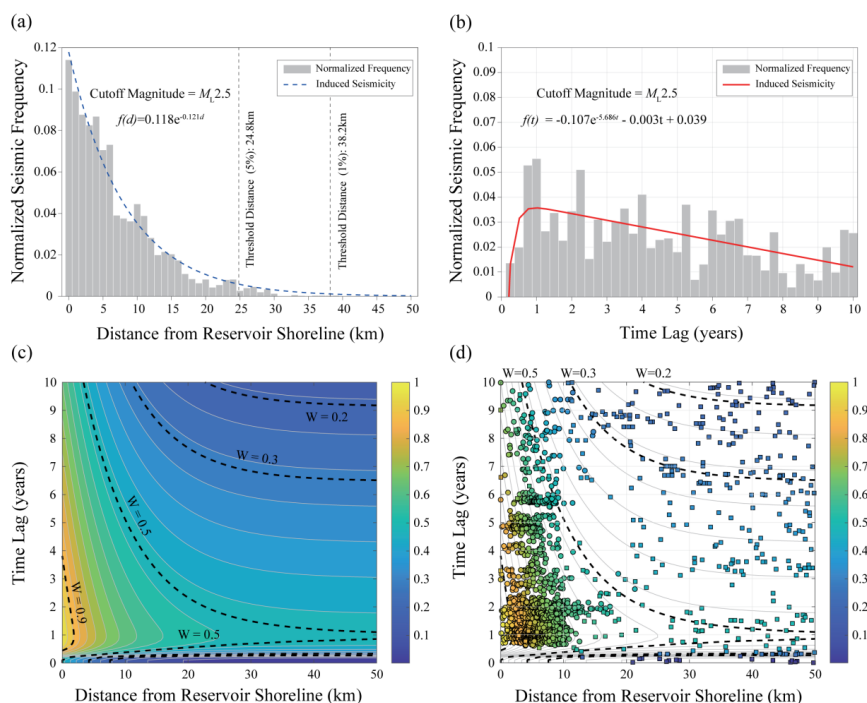
1004

1005 **Figure 2.** Spatial distribution characteristics of reservoir-induced seismicity in China. (a) Spatial
1006 distribution of large/medium-sized reservoirs and reservoirs with induced seismicity. Blue
1007 polygons represent large/medium-sized reservoirs (capacity $\geq 1 \times 10^8$ m³) with complete
1008 parameters (e.g., impoundment time, dam height); red polygons represent reservoirs with induced
1009 seismicity, identified based on spatiotemporal clustering. (b) Spatial density of reservoirs with
1010 induced seismicity (units: number per square degree). (c) Spatial distribution of the proportion of
1011 reservoirs with induced seismicity among all large/medium-sized reservoirs. (d) Density
1012 distribution of $M \geq 4.0$ earthquakes in China (units: number per square degree) and mapped active
1013 faults (brown lines).

1014

1015

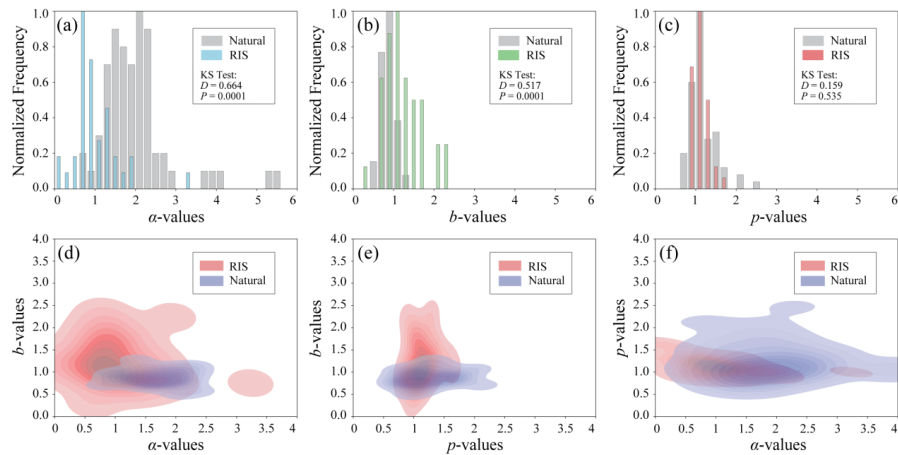
1016



1017

1018

1019 **Figure 3.** Spatiotemporal patterns of reservoir-induced seismicity and construction of the W-score
 1020 table. (a) Empirical distribution of normalized earthquake frequency versus distance from the
 1021 reservoir shoreline, with the blue curve showing the fit of a power-law function. (b) Empirical
 1022 distribution of normalized earthquake frequency versus time lag since initial impoundment, with
 1023 the red curve showing the fit of an exponential-linear hybrid model. (c) W-score table constructed
 1024 based on the joint distribution of reservoir distance and time lag. The color fill indicates the
 1025 probability of induced seismicity; black contour lines mark the boundaries for probabilities of 0.2,
 1026 0.3, 0.5, and 0.9. (d) Example application of the W-score table, using the Jinping-I Reservoir and
 1027 induced seismicity identification results for a completeness magnitude $M_c = M_L 2.5$. Circles
 1028 represent manually identified induced earthquakes, squares represent background earthquakes, and
 1029 the color fill indicates the probability of induced seismicity.



1030

1031

1032 **Figure 4.** Parameter characteristics of the reservoir-induced seismicity sequences. (a) Statistical

1033 distribution of the α -value from the ETAS model for the induced sequences. (b) Statistical

1034 distribution of the p -value from the ETAS model. (c) Statistical distribution of the b -value

1035 estimated using the OK1993 model. (d) Scatter plot of α -value versus b -value. (e) Scatter plot of

1036 p -value versus b -value. (f) Scatter plot of α -value versus p -value. In panels (d) to (f), the blue

1037 contours represent the bivariate kernel density estimate (KDE) for parameters of natural tectonic

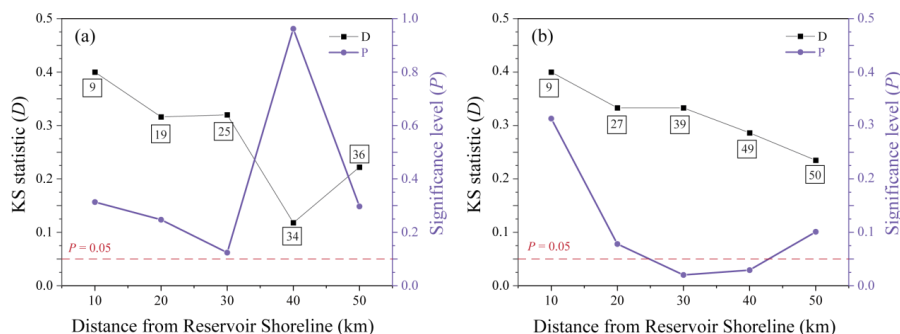
1038 seismicity sequences from previous studies, and the red contours represent the KDE for

1039 parameters of the induced seismicity sequences from this study.

1040

1041

1042



1043

1044

1045 **Figure 5.** Statistical characteristics of the Kolmogorov-Smirnov (KS) test comparing the b -values

1046 of induced sequences and background seismicity. (a) Zonal KS test results: b -values of

1047 background seismicity within concentric distance zones (0~10, 10~20, 20~30, 30~40, 40~50 km

1048 from the reservoir shoreline) are compared against the b -value of the induced sequence. The KS

1049 statistic (D) and significance level (P) are plotted against distance. (b) Cumulative zonal KS test

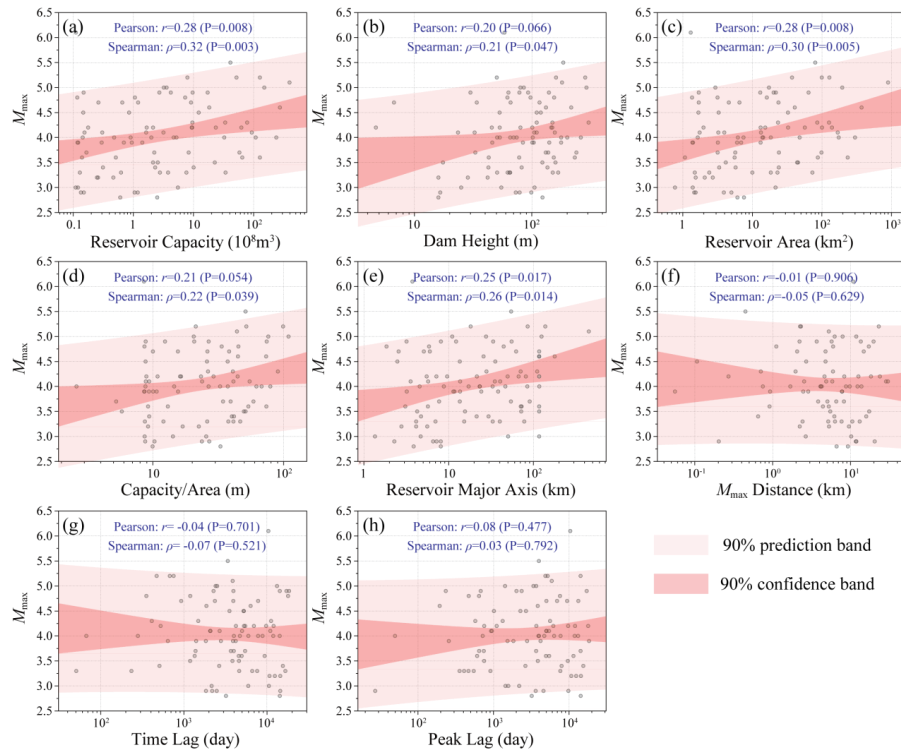
1050 results: based on b -values of background seismicity within cumulative distance ranges (0~10,

1051 0~20, 0~30, 0~40, 0~50 km). The red horizontal dashed lines in both panels indicate the statistical

1052 significance threshold ($P = 0.05$).

1053

1054



1055

1056

1057 **Figure 6.** Correlation analysis between the maximum magnitude (M_{max}) of induced seismicity and

1058 potential inducing factors. (a) Reservoir capacity (Reservoir Capacity, 10^8 m^3). (b) Dam height

1059 (Dam Height, m). (c) Reservoir surface area (Reservoir Area, km^2). (d) Mean water depth (Capacity

1060 / Area, m). (e) Reservoir major axis length (Reservoir Major Axis, km). (f) Distance from the

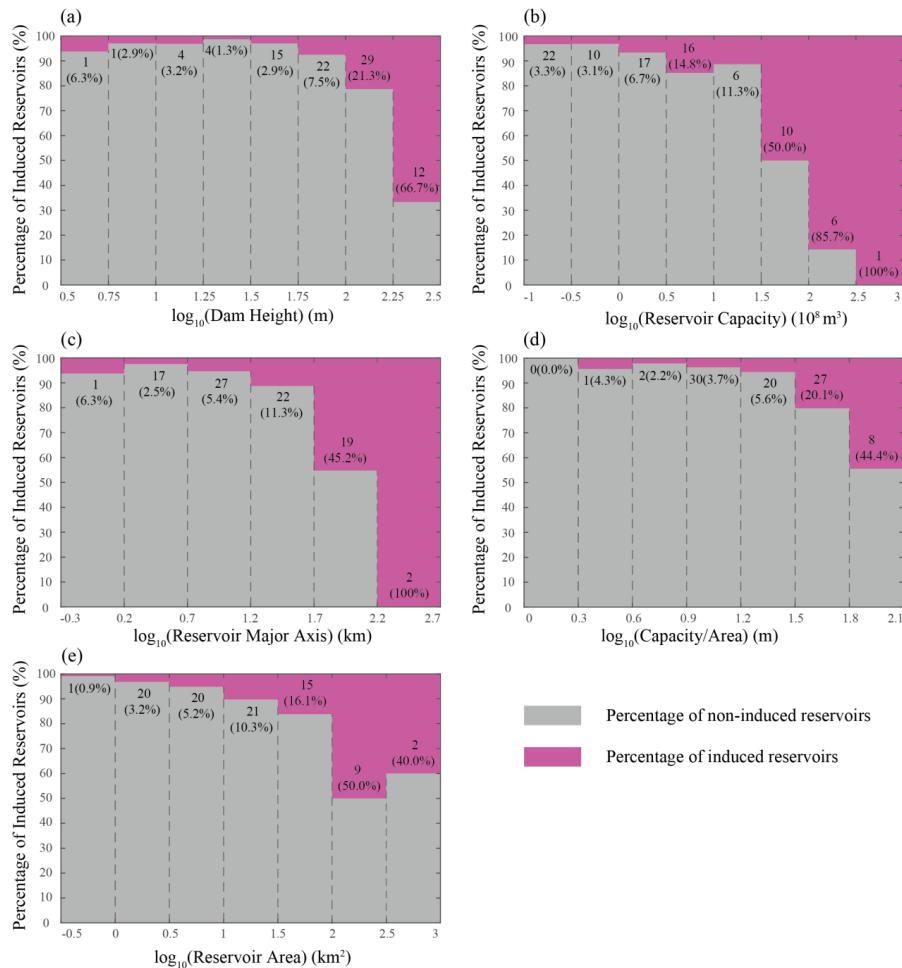
1061 reservoir shoreline of the M_{max} event (M_{max} Distance, km). (g) Time lag of the M_{max} event since

1062 initial impoundment (Time Lag, days). (h) Time lag of the peak seismicity rate since initial

1063 impoundment (Peak Lag, days). The Pearson correlation coefficient (r), Spearman correlation

1064 coefficient (ρ), and the corresponding significance level (P) are indicated textually in each subplot.

1065



1066

1067 **Figure 7.** Proportion characteristics of induced-type reservoirs under the influence of single factors.

1068 (a) Proportion across different bins of dam height (Dam Height, m). (b) Proportion across different

1069 bins of reservoir capacity (Reservoir Capacity, 10⁸ m³). (c) Proportion across different bins of

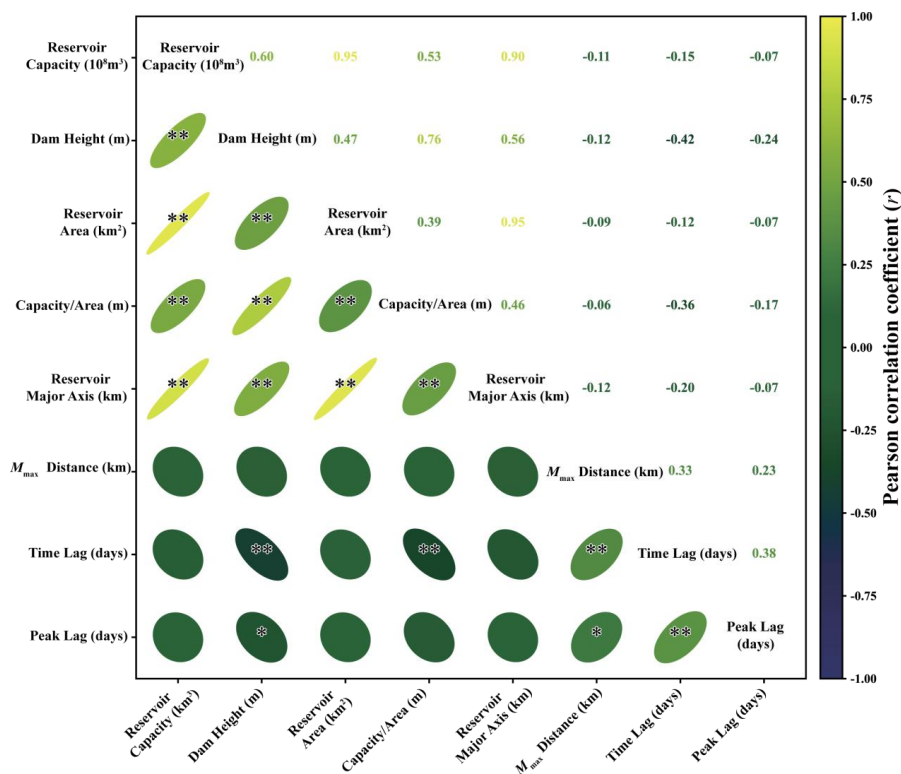
1070 reservoir major axis length (Reservoir Major Axis, km). (d) Proportion across different bins of mean

1071 water depth (Capacity / Area, m). (e) Proportion across different bins of reservoir surface area

1072 (Reservoir Area, km²). In each subplot, the purple filled area represents the proportion of induced-

1073 type reservoirs for the respective bin, and the gray filled area represents the proportion of non-

1074 induced-type reservoirs.



1075

1076

1077 **Figure 8.** Pearson correlation matrix among inducing factors. The lower triangle of the matrix

1078 visualizes the correlation coefficients using ellipses: flatter ellipses indicate stronger correlations; a

1079 45° tilt indicates a positive correlation, and a -45° tilt indicates a negative correlation; asterisks

1080 indicate the statistical significance level (* P<0.05, ** P<0.01). The upper triangle displays the

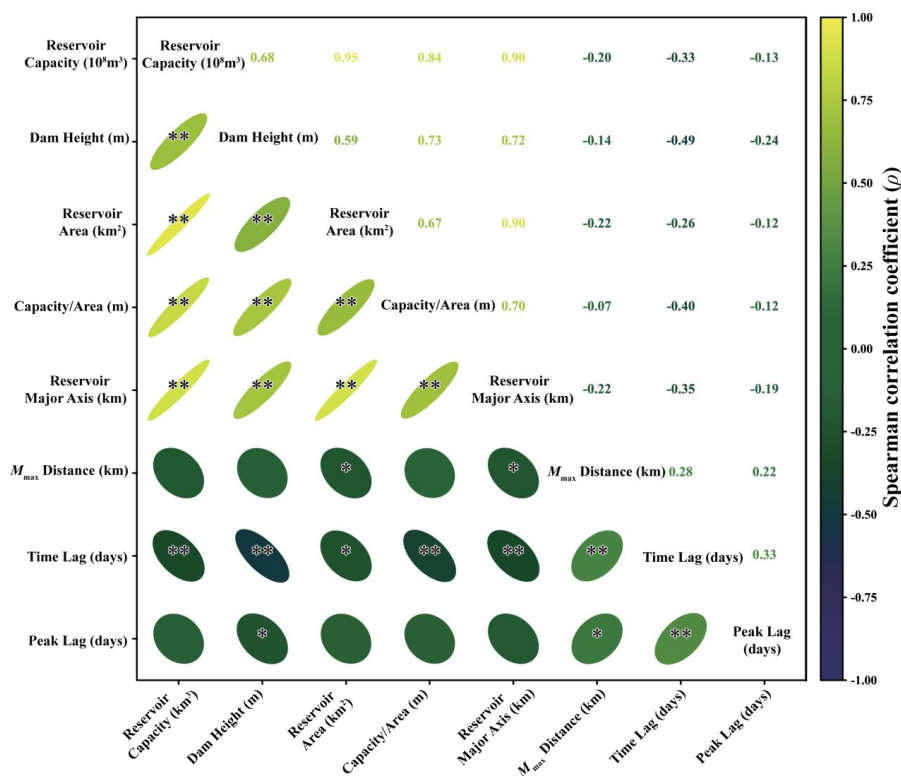
1081 Pearson correlation coefficient (*r*) numerically, with colors transitioning from blue (strong negative

1082 correlation) through green (weak correlation) to yellow (strong positive correlation). The inducing

1083 factors are: Reservoir Capacity (10⁸ m³), Dam Height (m), Reservoir Area (km²), Capacity / Area

1084 (m), Reservoir Major Axis (km), *M*_{max} Distance (km), Time Lag (days), Peak Lag (days).

1085



1086

1087

1088 **Figure 9.** Spearman correlation matrix among inducing factors. In the lower triangle of the matrix,

1089 ellipses visualize the rank correlation coefficients: flatter ellipses indicate stronger correlations; a

1090 45° tilt indicates a positive correlation, and a -45° tilt indicates a negative correlation; asterisks

1091 indicate the statistical significance level (* P<0.05, ** P<0.01). The upper triangle displays the

1092 Spearman correlation coefficient (ρ) numerically, with colors transitioning from blue (strong

1093 negative correlation) through green (weak correlation) to yellow (strong positive correlation). The

1094 inducing factors are the same as in [Figure 8](#).

1095

1096

1097